

Terahertz dielectric waveguides

Shaghik Atakaramians,^{1,3,*} Shahraam Afshar V.,² Tanya M. Monro,² and Derek Abbott³

¹Centre for Ultrahigh bandwidth Devices for Optical Systems (CUDOS), Institute of Photonics and Optical Science (IPOS), School of Physics, The University of Sydney, Sydney NSW 2006, Australia

²Institute for Photonics and Advanced Sensing, School of Chemistry and Physics, The University of Adelaide, Adelaide SA 5005, Australia

³School of Electrical & Electronic Engineering, The University of Adelaide, Adelaide SA 5005, Australia

*Corresponding author: shaghik.a@sydney.edu.au

Received February 12, 2013; revised May 8, 2013; accepted May 9, 2013; published July 3, 2013 (Doc. ID 185276)

Several classes of non-planar metallic and dielectric waveguides have been proposed in the literature for guidance of terahertz (THz) or T-ray radiation. In this review, we focus on the development of dielectric waveguides, in the THz regime, with reduced loss and dispersion. First, we examine different THz spectroscopy configurations and fundamental equations employed for characterization of THz waveguides. Then we divide THz dielectric waveguides into three classes: solid-core, hollow-core, and porous-core waveguides. The guiding mechanism, fabrication steps, measured loss, and dispersion are presented for the waveguides in each class in chronological order. The goal of this review is to compare and contrast the current solutions for guiding THz radiation. © 2013 Optical Society of America

OCIS codes: (230.7370) Waveguides; (130.2790) Guided waves;
(260.3090) Infrared, far
<http://dx.doi.org/10.1364/AOP.5.000169>

1. Introduction.	170
1.1. History of THz Waveguides	171
2. Characterization of THz Waveguides.	172
3. Metallic Waveguides	176
4. Dielectric Waveguides	179
4.1. Hollow-Core Waveguides/Fibers	181
4.2. Solid-Core Waveguides/Fibers	188
4.3. Porous-Core Waveguides	194
5. Conclusion and Final Remarks.	204
Acknowledgments	205
References and Notes.	205

Terahertz dielectric waveguides

Shaghik Atakaramians, Shahraam Afshar V., Tanya M. Monro, and Derek Abbott

1. Introduction

Terahertz (THz) or T-ray radiation bridges the gap between microwave and optical wavelengths [1,2]. Traditionally this region was explored using only passive detection for applications in astronomy. Exploration of the THz spectrum with active detection, using laboratory-based sources, only began to emerge in the mid-1980s, mainly because of technical difficulties involved in making efficient and compact THz sources [3–5]. Since this part of the spectrum is located between the technologically well-developed microwave and infrared (IR) spectral regions, the THz region is well poised to benefit from the generation and detection technologies emerging from both regions. Waveguides in the THz regime are no exception; i.e., several waveguide solutions based on technologies from both electronics and photonics have been explored. In pulsed laser-based systems, subpicosecond THz pulses cover a broad range of the frequency spectrum, and the THz band is loosely defined as 0.1–10 THz (0.03–3 mm wavelengths) [1]. Currently, THz systems predominantly utilize free-space propagation, where losses can be minimized. In order to achieve guidance with greater confinement, one needs to lower the frequency dependent loss and dispersion to enable undistorted propagation of subpicosecond pulses in waveguides.

There are several benefits in having low-loss and low-dispersion waveguides. The primary application of waveguides is to transport electromagnetic waves (and consequently information) from one point to another [6]. Waveguides have also been exploited as sensing and imaging probes [7,8], as the main medium of quantum-cascade lasers [9], to guide waves in subwavelength regimes (beyond the diffraction limit), and to offer tight confinement of the electromagnetic waves to the structure beyond the Rayleigh range [10,11]. The potential benefits for the THz region are similar. The foremost advantage is that the bulk optics used for manipulating THz radiation in free space can be replaced by waveguides in THz time-domain spectroscopy (TDS) systems. This will open up new opportunities in further development of compact THz systems and consequently lab-on-chip systems to create advanced biosensors [12]. The diffraction limited spot size can be reduced further, resulting in a resolution improvement over free-space THz imaging systems. Also, tight mode confinement can be achieved by exploiting waveguides with subwavelength features. This is beneficial for THz sensing applications, specifically for noninvasive and label-free molecular detection, and gas and liquid spectroscopy [13–15]. A minute sample (a few micro-liters volume for THz [16]) can be replaced in or at the vicinity of the waveguide where strong interaction with a THz pulse is achieved due to the existence of a large power fraction of the guided mode. Other THz devices such as the near-field scanning optical microscope, THz sources based on quantum-cascade lasers, imaging, and communication technologies, which revolve around THz waveguides, will have improved functionalities.

Nevertheless, selecting materials that are suitable for the fabrication of waveguides is one of the major barriers in advancing this field. While metals function well at microwave frequencies, they have high Ohmic losses in the THz regime. While polymers and glasses function well at IR and optical frequencies, they have unacceptable frequency dependent absorption losses in the THz region. Another significant barrier that limits the application of waveguides, especially in THz spectroscopy and communication systems, is group-velocity dispersion. Consequently, different frequency components of the broad THz spectrum travel with different group velocities leading to distorted pulse shapes. Metal waveguides experience strong dispersion near the cut-off frequency of the guiding mode unless they support transverse electric and magnetic (TEM) modes that have no cut-off frequency [17,18]. Dielectric waveguides suffer from material and waveguide dispersion. It has been shown that material dispersion is negligible in dielectric waveguides and the dominant dispersion is due to the waveguide structure [19]. Although waveguide dispersion can be tailored such that a flat (almost zero) dispersion region is achieved for a range of frequencies, it is not straightforward to design dielectric waveguides to offer zero dispersion for the entire broad THz spectrum. For applications that require a broad spectrum, such as general spectroscopic sensing, this is an issue. However, this may not be an issue for some applications, such as probing specific materials that have spectral features in a narrow frequency.

1.1. History of THz Waveguides

In the early 1980s, THz pulses (in the pico/subpicosecond regime) were generated and sampled by photoconductive switches, also known as Auston switches. These photoconductive switches were incorporated into microstrip [20,21] and coplanar (still used today) [22–24] transmission lines. A microstrip transmission line is a type of electrical transmission line that consists of a conducting strip separated from a ground plane by a dielectric substrate [25], while a coplanar transmission line is an alternative type of electrical transmission line that consists of a conducting strip on a dielectric substrate with two ground electrodes running adjacent and parallel to strip [26,27]. A limitation of the microstrip line configuration, in the THz system, was that such systems suffered from reflections (ringing) at the generation point. Also these microstrip-based THz systems had high dispersion due to the dielectric substrate [28]. In the coplanar transmission THz system, the generated subpicosecond pulse (0.6 ps, for example) undergoes lower distortion compared to microstrip lines [22]. Therefore, they are more suitable for far-IR spectroscopy [29]. The coplanar transmission line THz system suffers from strong frequency dependent loss due to Cherenkov-like radiation [24,30], which is equivalent to the loss process of leaky waveguides in the frequency domain [23,24]. The total observed loss owing to the dielectric and metal in microstrip and coplanar transmission lines in THz systems is very high. Examples of the reported loss for thin-film microstrip and coplanar transmission lines are $\alpha = 18 \text{ cm}^{-1}$ and $\alpha = 14 \text{ cm}^{-1}$ at 1 THz, respectively. The loss increases as frequency increases with f and f^3 dependence, respectively [31].

In the above-mentioned techniques for excitation and sampling of pico/subpicosecond pulses, the effects of intermediate transmission media need to be considered. The pulse traveling through these transmission media is distorted due to frequency dependent loss and dispersion [28]. In 1989, the first free-space

tightly coupled THz spectroscopy system was proposed by van Exter *et al.* [32], and the first sample investigated was water vapor [5,33]. The technique employed for generation and detection of subpicosecond pulses allows a very low-loss propagation of THz radiation in free space (almost zero loss and dispersion) and eliminates lossy planar waveguides. Optical hardware (e.g., mirrors and lenses) were and still are exploited for steering, focusing, and efficient coupling of the pulses between excitation and detection points. Moreover, waveguides offer stronger interaction between the sample and the THz radiation, as well as providing the ability to direct radiation to locations that are difficult to access (e.g., as in endoscopy). Waveguides can also confine the pulse in a subwavelength regime and/or focus the beam to a smaller spot size to beat the diffraction limit.

Thus a whole new era has begun in THz radiation guidance, where non-planar guiding techniques adapted from the microwave or optic fields have emerged. Nonetheless, in parallel there has been plenty of research conducted to improve the loss and dispersion mechanisms in coplanar waveguides, resulting in modified planar single-wire waveguides also known as Goubau transmission lines [34–37]. The focus on coplanar waveguides is due to the fact that such waveguides appear straightforward for integration of THz functions inside microfluidic circuits or to achieve on-chip THz circuitry. Note that planar transmission lines are not in the scope of this review.

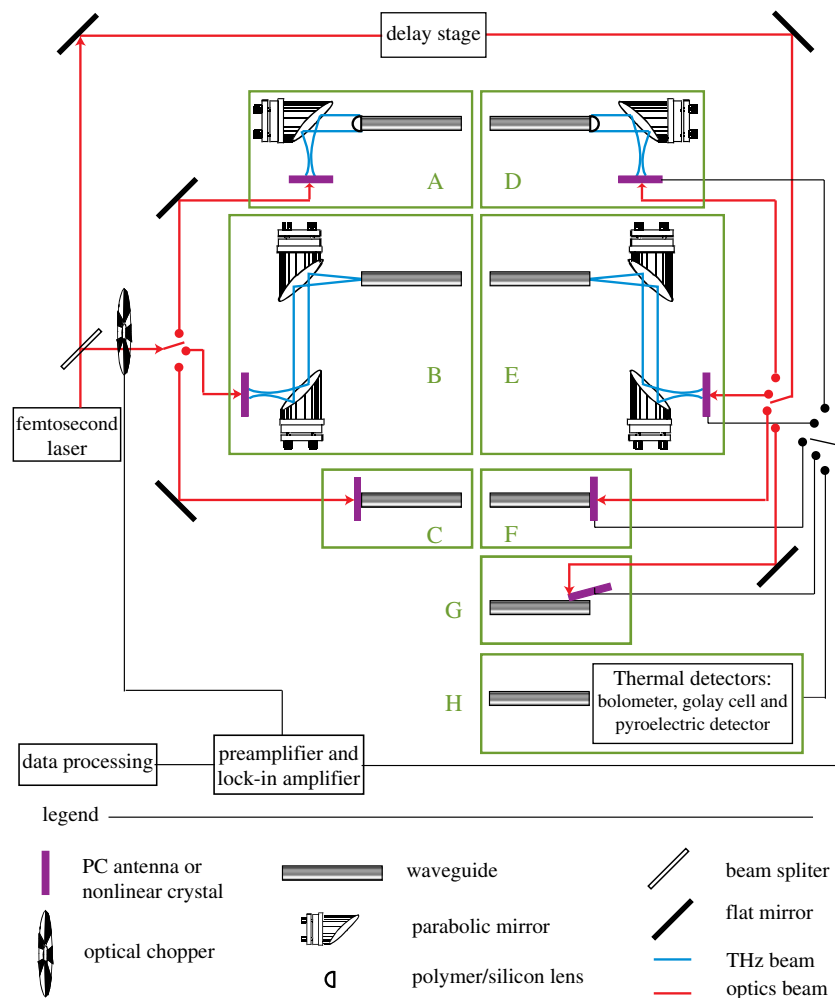
Several types of non-planar waveguides have been proposed in the literature for guiding within the THz spectrum to reduce frequency loss and dispersion. In this review, in Section 2, we define the key parameters used in the literature for characterization of THz waveguides. In the same section we overview different THz spectroscopy configurations and fundamental equations employed in the characterization of THz waveguides. In general, non-planar waveguides can be divided into two major categories: metallic and dielectric waveguides. Metallic waveguides proposed for THz radiation guidance are in general the scaled-down versions (in term of dimension) of well-known guiding devices from microwave and radio frequencies. Although metallic waveguides are not in the scope of this review, four types of metallic waveguides will be briefly discussed in Section 3. The four waveguides are discussed here, as they follow a trend of evolution similar to that of dielectric waveguides. Moreover, the metallic waveguides discussed in Section 3, except the first type that represents the first non-planar waveguide proposed in the literature, are among the best guiding structures proposed for this category. This has been carried out to allow the comparison of loss and dispersion parameters between the two categories of metallic and dielectric waveguides resulting in a wider picture of the THz waveguide arena. Dielectric fibers and waveguides, in the THz regime, can be considered as scaled-up versions of those used in the IR and optical frequency ranges. These waveguides are discussed in Section 4.

2. Characterization of THz Waveguides

In this review, the term *waveguide characterization* is used to imply the study of the loss and dispersion properties of the waveguide as a function of frequency/wavelength. Different arrangements of emitters, detectors, and THz optics (mirrors and lenses) can be utilized for characterization of a THz waveguide, which is summarized in Fig. 1. Usually photoconductive antennas and nonlinear

crystals are employed in the generation of THz pulses. The generated THz pulses are typically manipulated and focused employing parabolic mirrors and silicon/dielectric lenses, as seen in options A and B in Fig. 1. Silicon/dielectric lenses are used at the interface of the waveguide to achieve a smaller spot size at the front-end of the waveguide and consequently to increase the coupling into the waveguide. An alternative approach is positioning the waveguide on the emitter, shown by option C in Fig. 1, for coupling into the waveguide. As an example, McGowan *et al.* [31] and Mendis and Grischkowsky [18] used option A, Chen *et al.* [38], Ponseca *et al.* [39], and Lai *et al.* [40] used option B, and Jeon *et al.* [41], Wächter *et al.* [42], and Atakaramians *et al.* [43] used option C for coupling THz pulses into the waveguides. These waveguides are discussed in detail in Sections 3 and 4.

Figure 1



Schematic of the devices required for characterization of THz waveguides. The standard generation and coupling in techniques are shown in the left hand side of the figure (options A to C), while the detection and coupling out techniques are shown in the right-hand side of the figure (options D to H). Different combinations of these techniques can be employed for characterization of waveguides.

Similar arrangements to those used to couple into the waveguides are employed for coupling out the THz pulses from the waveguide, as shown in the right hand side (options D to F) of Fig. 1. Development of near-field photoconductive probes [44,45] has not only advanced THz near-field imaging, but has also allowed probing THz pulses along the waveguides. This approach, shown in option G in Fig. 1, is suitable for waveguides that have extended power outside the structure where the probe-tips can be positioned [46,47]. As an example, McGowan *et al.* [31], Gallot *et al.* [17], and Mendis and Grischkowsky [18] used option D, Ponseca *et al.* [39] used option E, Jeon *et al.* [41] and Wang and Mittleman [48] used option F, and Wächter *et al.* [42] and Atakaramians *et al.* [43] used option G for coupling THz pulses into the waveguides. All the detection methods (options D to G) discussed so far employ photoconductive detectors for measuring THz pulses. This approach is known as coherent detection. In this approach both the amplitude and the phase of the electric field and consequently the absorption coefficient (effective material loss) and effective refractive index of the propagating mode can be determined as a function of frequency. The relevant equations are discussed later in this section. Thermal detectors (e.g., bolometer and pyroelectric devices) are also employed to measure the intensity of the THz radiation, from which only the absorption coefficient of the propagating mode can be determined as a function of frequency. As an example, Chen *et al.* [38], Bowden *et al.* [49], and Lai *et al.* [40] used the thermal detection method (option H in Fig. 1) for coupling THz pulses into the waveguides. All these waveguides are discussed in detail later in Sections 3 and 4.

Any combination of options A to C and options D to H in Fig. 1 can be used for the characterization of THz waveguides. The waveguides are mostly characterized in transmission mode; i.e., the THz pulse is launched into the waveguide from one end and coupled out and measured from the other end. To date only one reflection mode characterization technique has been reported [50], where the THz pulses are coupled into and out of the fiber from one end, and a metal plate is positioned at the end of the fiber to reflect the beam.

In general, two different methods have been used for the characterization of THz waveguides. In the first approach, two pulses are measured: a reference pulse when all the steering and coupling devices are in the system except the waveguide, and a sample pulse when the waveguide is also included in the system. The loss and dispersion parameters are calculated from these two measurements. For example, [17,18,31,51] have used this approach for characterization of THz waveguides. In the second approach, THz pulses propagating through a minimum of two different lengths of a waveguide are measured and compared, where the loss and dispersion parameters are calculated. This method for characterization of waveguides is known as the cut-back technique and is used primarily for characterization of fibers in optics [52]. In this technique the waveguide is situated in the system and the propagating pulses are measured at the output. Later the waveguide is cut down from the output end so that the coupling in arrangement is maintained and the propagating pulses are measured once more. This can be repeated as many times as desired. Since the waveguide is cut down for each measurement, this technique is called the cut-back technique. For example, [23,38,53] have used this approach for characterization of THz waveguides.

Coherent detection allows one to measure the complex electric field, i.e., amplitude and phase. As the sample under investigation is placed in the system,

assuming single-mode propagation, the equation governing the input and output electric fields of the sample can be written in the frequency domain as [23]

$$E_{\text{out}}(\omega) = E_{\text{ref}}(\omega) T_1 T_2 C^2 \exp(-\alpha L/2) \exp(-j\beta_0 n L), \quad (1)$$

where $E_{\text{out}}(\omega)$ and $E_{\text{ref}}(\omega)$ are the complex electric fields at angular frequency ω on the entrance and exit of the waveguide, respectively; T_1 and T_2 are the total transmission coefficients that take into account the reflections at the entrance and exit faces, respectively; C is the coupling coefficient, the same for the entrance and exit faces; β_0 is the free-space phase/propagation constant; n is the refractive index of the sample; α is the power absorption coefficient; and L is the thickness/length of the sample. The generated THz electromagnetic wave is a linearly polarized plane wave. When passing through a sample with a large cross section (larger than the operating wavelength), it still remains plane wave. However, when the sample under investigation is a waveguide, the impinging plane wave is coupled into the propagating modes of the waveguide so that it can be carried along the waveguide. Thus when the sample under investigation is a waveguide, the refractive index of the sample, n , and power absorption coefficient, α , in Eq. (1) should be replaced respectively by the effective refractive index, n_{eff} , and the effective material loss, α_{eff} , of the mode propagating through the waveguide. Thus Eq. (1) becomes

$$E_{\text{out}}(\omega) = E_{\text{ref}}(\omega) T_1 T_2 C^2 \exp(-\alpha_{\text{eff}} L/2) \exp(-j\beta_{\text{eff}} L), \quad (2)$$

where $\beta_{\text{eff}} = \beta_0 n_{\text{eff}}$ is the propagation constant of the propagating mode, and α_{eff} is the effective material loss that the propagating mode experiences.

To attain the absorption coefficient (α_{eff}) and/or effective refractive index (β_{eff}) values of a waveguide, THz pulses propagating through different lengths of a waveguide are measured. Applying Eq. (2) to a minimum of two different lengths (L_1 and L_2), the transfer function determined from the ratio of $E_{\text{out1}}(\omega)$ and $E_{\text{out2}}(\omega)$ reads as

$$\frac{E_{\text{out1}}(\omega)}{E_{\text{out2}}(\omega)} = \exp(-\alpha_{\text{eff}}(L_1 - L_2)/2) \exp(-j\beta_{\text{eff}}(L_1 - L_2)). \quad (3)$$

The C , T_1 , and T_2 coefficients are canceled provided that the positions of the waveguide and emitter do not change as would occur during a cut-back measurement. Then α_{eff} and β_{eff} of the waveguide can be obtained from the amplitude and the phase of the transfer function [Eq. (3)]. As we shall see later on, the *in situ* cleaving of THz waveguides is complicated. Two techniques have been employed to reduce the coupling coefficient uncertainty. The first uses near-field probe-tips (option G in Fig. 1) to sample along the waveguides. In this case the probe moves across the waveguide and no cleaving is required. In this approach the distance of the probe-tip from the waveguide should be monitored and kept constant. This is only applicable to waveguides in which the propagating mode extends outside the structure. The second involves measuring waveguides with different lengths. In this approach different waveguide lengths are positioned in the system. The coupling in and out may vary from measurement to measurement, indicating that the transfer function determined from the ratio of $E_{\text{out1}}(\omega)$ and $E_{\text{out2}}(\omega)$ cannot be simplified to Eq. (3). Note that the waveguide can still be characterized by averaging several scans, while the position of the waveguide

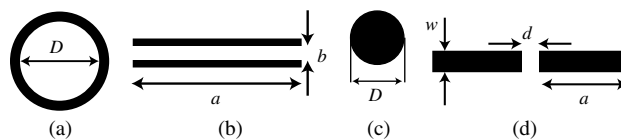
slightly changes for each case to compensate for the variation of the coupling changes from each waveguide measurement.

3. Metallic Waveguides

Metallic waveguides proposed for THz radiation guidance are mostly scaled-down versions (in terms of dimension) of well-known guiding devices from microwave and radio frequencies. The electromagnetic waves at THz frequencies are not as dissipative in metallic components as they are for higher frequencies such as visible light. Thus metallic structures still can be used for guidance in this regime. Hollow metallic circular/rectangular waveguides [17,31], parallel-plate waveguides [18,54–56], coaxial waveguides [57], metal wire waveguides [41,42,48], parallel-plate photonic waveguides [58], metal sheet waveguides [59], and metallic slot waveguides [46] are examples of metallic waveguides proposed for guidance of the THz spectrum. Although metallic waveguides are not in the scope of this review, four types of metallic waveguides are briefly discussed in this section. We start this section with metallic circular waveguides since they are the first non-planar waveguides proposed for guidance of THz radiation. Moreover, hollow-core hybrid-clad waveguides, which are discussed in Section 4.1, are the modified version of these waveguides. Then we proceed to parallel-plate waveguides, and bare metal wire and slit waveguides, where the tradeoff between loss and confinement becomes apparent. As we shall observe later, dielectric waveguides have evolved in a similar way.

Circular cross-section waveguides. Metallic waveguides with circular cross sections, as shown in Fig. 2(a), were among the first experimental investigations conducted using quasi-optical methods to couple freely propagating THz pulses [31]. In 1999, McGowan *et al.* [31] demonstrated that circular waveguides have lower loss ($\alpha = 0.7 \text{ cm}^{-1}$ at 1 THz) relative to coplanar and microstrip transmission lines ($\alpha = 14 \text{ cm}^{-1}$ and $\alpha = 18 \text{ cm}^{-1}$, respectively). This is due to the fact that the propagating THz pulses experience only Ohmic losses due to the metallic body of the circular waveguide, while they suffer from three different loss mechanisms when propagating via transmission lines, i.e., Ohmic losses due to metal strips, dielectric losses due to substrate, and radiative losses. However, THz pulses propagating through a circular waveguide experience strong dispersion near the cut-off frequency associated with the fact that the transmitted THz pulse through these waveguides is stretched with the higher frequencies arriving earlier in time, i.e., a negative chirp. As an example, a

Figure 2



(a) Circular metallic waveguide, indicating the diameter, D . (b) Parallel-plate waveguide, indicating the width of the plates, b , and the separation of the plates, a . (c) Bare metal wire, indicating the wire diameter, D . (d) Metallic slot waveguides, indicating the plates' width, w , the plates' length, a , and the plates' separation, d .

≈ 1 ps duration THz pulse after propagating 25 mm through a 280 μm diameter circular brass waveguide stretches to ≈ 40 ps [17]. It was also demonstrated both theoretically and experimentally that rectangular metallic waveguides have similar losses to circular waveguides, for 0.65–3.5 THz bandwidth [17].

Parallel-plate waveguides. The guiding structure consists of two parallel conducting plates positioned close together (108 μm gap in between the plates for THz [18]), as shown in Fig. 2(b). The structure supports single TEM mode propagation, which is the lowest-order TM mode: TM_0 . The TEM mode has no cut-off frequency. Thus, unlike the circular and rectangular metallic waveguides that suffer from extreme broadening of the THz pulse near the cut-off frequencies, the parallel-plate waveguide has no group-velocity dispersion [51]. Moreover, the electric field of a parallel-plate waveguide is linearly polarized and perpendicular to the plates. This facilitates the coupling of linearly polarized THz pulses into the structure. An attenuation constant less than 0.3 cm^{-1} and with almost no pulse broadening (zero dispersion) is observed for a parallel-plate waveguide within the bandwidth from 0.1 to 4 THz [18]. The Ohmic losses due to the finite conductivity of the plates and divergence losses due to beam spreading in the unguided direction are the main loss mechanisms in these waveguides.

The TE_1 mode is the second higher-order mode that can be excited in the parallel-plate waveguide [55,56]. The TE_1 mode is excited if the input beam is polarized parallel to the plates, while the TEM mode is excited when the input beam is polarized perpendicular to the plates. The selection of which mode to excite in parallel-plate waveguides depends on the application. As an example, the TE_1 mode can be exploited for excitation of a simple resonant cavity integrated with a parallel-plate waveguide, which cannot be excited by the TEM mode [56]. Because of the almost zero dispersion and low-loss characteristics of the parallel-plate waveguide, this waveguide has also been used in applications such as sensing, imaging, and signal processing [16,55].

Bare metal wires. The bare metal wire, also known as a Sommerfeld wire, is a single cylindrical conductor (wire), as shown in Fig. 2(c). Electromagnetic waves propagate as weakly guided radial surface waves along an infinitely long wire of circular cross section, due to the finite conductivity of the metal, and are called surface plasmon waves. Only the principal mode, a radially symmetric transverse magnetic wave (TM_{01}), travels along the wire and has remarkably low loss and low group-velocity dispersion, whereas all other modes have high attenuation, which makes the wire effectively single mode [60]. The guided surface wave and the single wire are respectively called the Sommerfeld wave and the Sommerfeld wire, because Sommerfeld found the first rigorous solution of Maxwell's equations, for wave propagation on a single wire [41,42,48]. In comparison to other metallic waveguides, the exposed metal surface area to propagating THz pulses is reduced, leading to lower Ohmic losses. As an example, it is reported that a 0.9 mm diameter stainless steel wire has an attenuation constant less than 0.03 cm^{-1} and almost zero dispersion from 0.25 to 0.75 THz [48].

The mode propagating along a single wire largely extends into the surrounding air. The wire acts as a rail for the guiding mode, which is analogous to optical nanowires and THz microwires (Section 4). This makes the coupling in between

the wires simple; i.e., the THz pulses can be coupled into a wire if it is positioned in the extended field of another wire. Despite its superior transmission behavior, the bare metal wire suffers from radiation losses. Any perturbation of the structure, e.g., bending, or even in the vicinity of the wire (within the region of the extended field) leads to high radiation losses due to the loose confinement of the mode to the structure. Coating the wire with a dielectric is an approach to improve the confinement. However, for the THz spectrum, the dielectric coating introduces frequency dependent loss to the propagating mode [42].

Metallic slot waveguides. Wächter *et al.* [46] proposed metallic slot waveguides for the guidance of THz radiation to increase the field confinement to the waveguide compared to the metal wire. The structure was made up of two planar slabs ($20\text{ mm} \times 300\text{ }\mu\text{m}$) located $d = 270\text{ }\mu\text{m}$ apart from each other, as shown in Fig. 2(d). Compared with the bare metal wire, the electromagnetic fields are more confined to the slot waveguide (more than 50% of guided mode power is within the area not exceeding one wavelength around the slot waveguide, while this number is less than 22% for bare metal wire [46]). However, the attenuation loss of slot waveguides is higher than metal wires. The propagating mode in a slot waveguide is in contact with a larger metal area compared to that of a metal wire, leading to higher attenuation losses for the slot waveguide. The attenuation constant of a slot waveguide made from silicon wafer coated with Ti and Au is less than 0.07 cm^{-1} in the frequency range 0.1–1 THz with almost zero dispersion [46].

Four different metallic structures have been reviewed in this section. Metallic waveguides with circular cross sections: the propagating mode (TE and/or TM modes) is tightly confined in the structure (metallic walls) leading to high losses due to finite conductivity of the metals in THz frequencies. The propagating mode inside these metallic waveguides suffers from high dispersion near the cut-off frequency of the mode. Parallel-plate waveguides: the propagating mode (TEM) is still confined in between the plates in one direction with a lower attenuation constant compared to circular and rectangular metallic waveguides. In addition to lower loss, these waveguides offer dispersion-free propagation. Bare metal wire: the conducting (Ohmic) loss is reduced considerably since the wire acts as a rail for the guided mode (TM_{01}). The mode is loosely confined to the wire and is expanded to the surrounding medium (air), resulting in low-loss and dispersion-free propagation of THz pulses. Metallic slot waveguide: the THz pulses still propagate in air with a higher confinement to the waveguide compared to metal wire and nearly no dispersion. The confinement leads to higher loss for the slot waveguide compared to metal wire, indicating there is a tradeoff between strong mode confinement and low attenuation in metallic waveguides. As we shall observe in the next section, there is a similar tradeoff for dielectric waveguides.

4. Dielectric Waveguides

Another major category of non-planar waveguides proposed for the THz spectrum is dielectric waveguides. These waveguides are also known as fibers if they are flexible and have circular cross sections and are mostly used at higher frequencies, such as IR and optical frequencies, where metallic waveguides are dissipative.

Dielectric waveguides suffer from material absorption since suitable dielectric materials for fabrication of waveguides are lossy. Although high-resistivity silicon has extremely low loss ($\alpha < 0.05 \text{ cm}^{-1}$ for frequencies below 2.5 THz [61]), it is not amenable for fabrication of many waveguide geometries. The material choice and waveguide structure have a great impact on the waveguide performance, not only on transmission loss but also on dispersion. Table 1 shows the bulk material absorption and refractive index of low-loss polymers that have been used to fabricate THz waveguides. As can be observed, polymethyl methacrylate (PMMA) and polycarbonate (PC) have relatively higher losses compared to those of high-density polyethylene (HDPE) and polytetrafluoroethylene (PTFE, best known as Teflon). It should be noted that the material properties listed here are based on published results [62–65], and these values could differ slightly depending on the material supplier [62]. Among the polymers listed in this table, cyclic olefin copolymer (COC), commercially known as TOPAS and Zeonex, has the lowest material absorption losses in the THz range. The refractive index of these polymer materials is in the range of 1.4–1.7. These polymer materials have been widely used as host materials for THz waveguides, as filling materials (materials that are combined with the sample under investigation to exclude saturation of the strong absorption modes) to increase the dynamic range of the measurement, and as a sample cell window material for liquids and gases in the THz range. There are no dielectric materials with negligible absorption in the THz spectrum except for air. Thus, where possible, air is usually the material of choice as the core material for THz bandgap waveguides.

The dielectric waveguides proposed for THz guidance can be divided into three classes: hollow-core, solid-core, and porous-core waveguides. The guiding

Table 1. Material Properties of Most Common Polymers Used for THz Waveguides^a

Polymer	Absorption	Refractive Index	Refs.
PMMA polymethyl methacrylate	$<20 \text{ cm}^{-1}$	1.5–1.6	[62–64]
PC polycarbonate	$<10 \text{ cm}^{-1}$	1.63–1.67	[63,64]
PTFE polytetrafluoroethylene	$<0.9 \text{ cm}^{-1}$	1.43–1.44	[62,64]
HDPE high-density polyethylene	$<0.4 \text{ cm}^{-1}$	1.5–1.56	[63,64]
COC cyclic olefin copolymer	$<0.25 \text{ cm}^{-1}$	1.51–1.53	[62,64]

^a The material properties are for $f \leq 1 \text{ THz}$.

mechanism for each class of structure is different. The guiding mechanisms in all-dielectric hollow-core waveguides come from formation of either photonic bandgaps or antiresonances with the immediate cladding structure. If the waveguides have an inner metallic coating, then the mode is guided via reflection from the metal coating, which presents a highly reflective mirror. On the other hand, the guiding mechanisms in solid-core and porous-core waveguides are based on total internal reflection if the average refractive index of the core is greater than that of the cladding (e.g., air-clad). When the average refractive index of the core is smaller than that of the cladding, the guiding mechanism is via formation of the photonic bandgap [66]. To the best of our knowledge, there is only one case—the porous-core bandgap waveguide—theoretically reported for the THz spectrum [67]. Table 2 summarizes the guiding mechanism for each class and type of dielectric waveguides.

The fabrication process of dielectric waveguides has benefited from the advance fabrication process of optical waveguides, especially microstructured optical fibers (MOFs) and IR waveguides. The fabrication techniques for MOFs usually have two stages. The first stage is the fabrication of a fiber preform, which is the scaled-up version of the fiber. In the second stage, the fiber preforms are drawn to fibers often via a caning stage to provide a central core region with smaller-scale structure. There are a range of techniques available for fabrication of MOF preforms: stacking of capillary tubes, drilling holes in the bulk material, casting into a microstructured mold, and extrusion [68]. On some occasions, due to the larger dimension of THz waveguides compared to that in the optics, the fabrication of waveguides encountered fewer steps. As we shall observe in this section, for THz hollow-core and solid-core microstructured waveguides, the waveguide preform by itself is suitable for THz guidance, resulting in the elimination of the second stage in the fabrication process, i.e., the drawing process [69–71]. In the area of fabrication of THz waveguides, there are also some techniques borrowed from fabrication of hollow-core IR waveguides [72], e.g., using a sputtering ring chamber or wet-chemistry technique to deposit metallic/dielectric layers on/inside a tube.

Here, we first review hollow-core waveguides in Subsection 4.1, for which the THz pulses are guided in the hollow core of the waveguide. In Subsections 4.2 and 4.3, we respectively review solid-core waveguides and porous-core waveguides. The common feature in these classes of dielectric waveguides is that the average refractive index in the core is higher than the average refractive index of the cladding, leading to total internal reflection as the guiding mechanism. For each part, we first explain the guiding mechanism, and then the measured loss and dispersion values. In cases in which an experiment is not conducted, we discuss the simulated loss and dispersion values. Moreover, the waveguide fabrication and characterization techniques are discussed.

Table 2. Summary of Guiding Mechanism of Dielectric Waveguides

Waveguide Class	Cladding Type	Guiding Mechanism
Hollow-core	Single/hybrid microstructured	Metal: reflection dielectric: antiresonance formation of bandgap antiresonance
Solid-core	Air microstructured	Total internal reflection formation of bandgap ^a
Porous-core	Air microstructured	Total internal reflection formation of bandgap ^a

^a When the average refractive index of the core is smaller than that of the cladding.

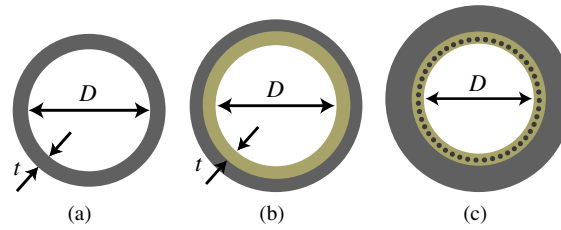
4.1. Hollow-Core Waveguides/Fibers

Guiding the mode through the hollow core is the common feature of waveguides in this class. In general, the guiding mechanisms in all-dielectric hollow-core waveguides are either via formation of photonic bandgaps or due to antiresonances with the immediate cladding structure (typically the inner core ring and struts) [73,74]. The cladding features (the inner ring and struts) resonantly reflect the mode back into the core, and the cladding thickness dictates the width of the transmission bands. In the former guiding mechanism, the cladding does not support modes for certain ranges of frequency, so the guided modes stay in the core. Waveguides such as microstructured bandgap fibers [75,76] and Bragg fibers [77,78] are two well-known examples of this class in optics. In the latter guiding mechanism, there is a low overlap between the core guided modes and cladding modes by virtue of the low density of states in the cladding, which leads to confinement of the mode in the core. Kagomé [79,80] and square [81,82] lattice hollow-core microstructured fibers, in which the guiding mechanism is due to the antiresonance effect of the lattice, are the well-known examples in this class. There is a strong relationship (continuous mapping via a tight-binding picture) between the bandgap and antiresonance description in 1-D structures [83,84].

For the THz frequency range, the material absorption of hollow-core waveguides is low since the THz radiation is predominately concentrated in the air core, which is transparent to THz radiation. However, as we observe for each waveguide below, the dimensions of these waveguides are in the order of a few millimeters, thus making them inflexible structures. Generally, we also observe that for such a broad THz spectrum, these waveguides are narrow-band; i.e., the transmission is limited to selected frequency bands due to the guiding mechanisms. Here, this class of THz waveguides is divided into three types: single/hybrid-clad waveguides, microstructured bandgap waveguides, and Kagomé microstructured waveguides. For the first type, waveguides with one or more cladding layers (layers that are usually added to reduce the loss by changing the type of propagating mode) are discussed. Then waveguides with microstructured cladding are discussed and have been divided into two types (bandgap and Kagomé) based on their guiding mechanism.

Hollow-core single/hybrid-clad waveguides. As discussed in Section 3, metallic waveguides with circular cross sections were among the early non-planar waveguides purposed for THz guidance [31]. These waveguides had low transmission efficiency and strong dispersion near the cut-off frequencies, and were rigid. In 2003 Hidaka *et al.* [85] proposed a hollow-core THz waveguide made of ferroelectric poly vinylidene fluoride (PVDF), a flexible polymer, to increase the transmission coefficient. Such waveguides are considered as single clad waveguides, as shown in Fig. 3(b), in this review. The frequency dependent dielectric constant of PVDF has a resonance frequency in the THz range; i.e., the dielectric constant of the PVDF becomes negative for frequencies larger than 0.3 THz. This results in an imaginary refractive index like that in metals. With an imaginary refractive index, the material shows complete reflection like metals (close to unity) for both TM and TE polarization from 1 to 2 THz [86,87]. Compared to metals such as Cu, the reflectivity of TM polarization of PVDF is even higher in this frequency range. This leads to a three times larger transmission coefficient for an 8 mm bore diameter PVDF pipe ($\alpha = 1.5 \text{ m}^{-1}$) compared to that of a similar Ni-Cu pipe ($\alpha = 5 \text{ m}^{-1}$). For loss measurement of

Figure 3



(a) Hollow-core single clad waveguide, indicating the diameter, d , and the dielectric/metal thickness, t . Hollow-core hybrid-clad waveguides: (b) metal waveguides with dielectric inner coating, indicating the diameter, d , and the dielectric thickness, t . (c) Metal waveguides with a thin layer of metamaterial (metal wires in dielectric) as its inner cladding.

waveguides, a broadband THz radiation is generated by a nonlinear optical crystal, and an Si bolometer in liquid He is used as the THz detector.

Hollow-core waveguides with hybrid cladding were also proposed to lower the attenuation coefficient of the propagating modes, i.e., the loss. Here, hybrid-clad waveguides refer to structures with a minimum of two different clad layers. Each clad layer can be a simple material layer [e.g., dielectric coating as shown in Fig. 3(b)] or a composite material layer [e.g. metamaterial as shown in Fig. 3(c)] [88]. Generally, each layer has special properties (functionality) and contributes to the propagation of the mode. However, there are cases in which the cladding layer acts only as the supporting base for the next layer [89–91].

A common layer employed in hybrid-clad THz waveguides is a metal layer by virtue of its superior reflecting surface for TE modes [89,90]. This approach was adapted from IR metal-coated hollow glass waveguides [72]. When the thickness of the metal film is greater than the skin depth of the metal at THz, the hollow-core waveguides with an inner metal coating perform like metal waveguides with a circular cross section (metal pipe). In contrast to metal waveguides, these hollow-core waveguides are flexible and have a smoother and homogeneous inner surface. A hollow-core PC waveguide with Cu inner coating [89] and a hollow-core glass waveguide with silver coating [90] are the examples proposed for THz guidance. These hollow-core waveguides were fabricated using techniques adapted from hollow-core IR waveguides [72]. The lowest loss reported for the hollow-core PC waveguide with Cu inner coating was 3.9 dB/m (0.9 m^{-1}) at 1.89 THz ($\lambda = 158.51 \text{ }\mu\text{m}$) [89], and for the hollow-core glass waveguide with Ag inner coating it was around $\approx 8 \text{ dB/m}$ (1.8 m^{-1}) for 1.25–1.65 THz [90]. A tuneable parametric oscillator with an MgO:LiNbO₃ crystal was used as a THz source, and an Si bolometer was used as a THz detector.

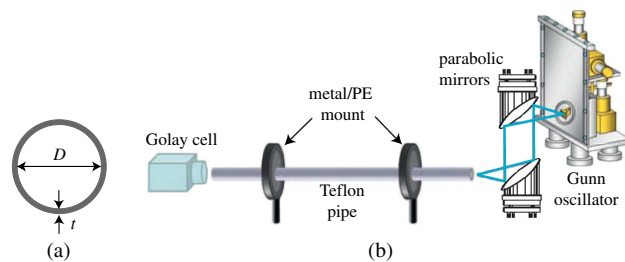
In hollow-core metal waveguides, the TE₁₁ mode is the propagating mode and is excited with the linearly polarized THz pulses. However, it is not the mode with the lowest attenuation constant in the metal waveguides. The TE₀₁ mode has the lowest loss (attenuation constant) with a doughnut-shaped mode distribution that cannot be launched easily with linearly polarized THz pulses.

To reduce the loss further in these hybrid-clad waveguides, a dielectric coating can be added [49,92,93]. This coating lowers the attenuation constant of the

TM modes and allows hybrid mode propagation. Thus the HE_{11} mode becomes the dominant mode with a lower attenuation constant. An important parameter in the design of dielectric coated hollow-core waveguides is the thickness of the dielectric coating, which determines whether the TE_{01} or HE_{11} mode has the lowest loss. A drawback of introducing the dielectric layer in the metallic waveguides is that the dielectric coating introduces interference peaks, which limit the bandwidth of operation [92]. Therefore the thickness of the dielectric coating should be designed so that the low-loss transmission window is located in the desired frequency region. Another drawback of dielectric coatings is that the inner dielectric coating adds absorption losses. Therefore, dielectric materials with low absorption losses ($\kappa = 2\pi\alpha/\lambda$ less than 0.065 [92]) should be selected in order to achieve lower losses in a hollow-core waveguide with inner dielectric coating compared to a metallic hollow-core waveguide. Loss of 0.22 m^{-1} (0.95 dB/m) at 2.5 THz (119 μm) is reported for the fundamental mode of a silver/polystyrene (Ag/PS) coated hollow glass waveguide [49], and 0.32 m^{-1} (1.3 dB/m) at 1.5 THz (200 μm) is reported for a PE/Ag loaded hollow glass tube [92].

To reduce the losses further, a hollow-core waveguide with one thin layer of dielectric material as its cladding—the hollow pipe single polymer ring, as shown in Fig. 4(a)—has been proposed for THz guidance [40,94]. Unlike metallic/PVDF pipes, and hybrid-clad pipes (discussed above), where the guiding mechanism is due to highly reflective mirrors, the guiding mechanism in these polymer hollow pipes is based on the antiresonance guiding mechanism. This waveguide can be viewed as a simplified Kagomé-lattice waveguide (discussed later here) reduced to one layer of cladding, and the mode is guided based on the antiresonance guiding mechanism [95]. Lai *et al.* [40] have shown that with the single low-index dielectric layer (0.5 mm thickness), an attenuation constant of less than 0.02 cm^{-1} with almost 200 GHz bandwidth is achievable. The experimental setup used for characterization of the pipe waveguide is shown in Fig. 4(b). Two tunable continuous-wave Gunn oscillator modules with 0.32 to 0.46 THz and 0.405 to 0.52 THz frequency ranges and a Golay cell are used as the emitter and detector, respectively.

Figure 4



(a) Teflon low-index pipe waveguide, indicating the diameter, D , and the Teflon thickness, t . (b) Experimental setup used for characterization of low-index pipe waveguide. Two tunable continuous-wave Gunn oscillator modules are used as the THz emitter. The THz radiation is coupled into the structure with a pair of parabolic mirrors. A Golay cell is used as the THz detector. Reproduced with permission, ©2009. Optical Society of America [40].

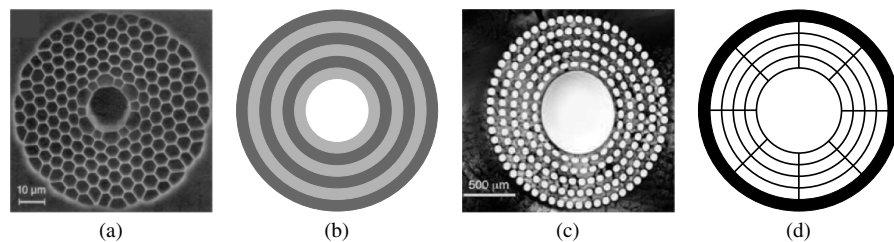
Due to the large core diameter (larger than operating wavelength), these hollow pipe waveguides suffer from multimode propagation, and they are not flexible. Moreover, higher-order modes are easily excited, especially at bends or small discontinuities.

Hollow-core microstructured bandgap waveguides. Hollow-core microstructured bandgap waveguides consist of a hollow core surrounded by micrometer-scale air holes in the cladding, which run along the length of the waveguide. The mode confines and propagates in the core when the cladding does not support the mode; i.e., the cladding forms a two-dimensional photonic crystal and the excited mode lies in the bandgap of the cladding. They were first proposed, developed, and optimized for visible and IR regimes [75,76,96]. A scanning electron microscope image of an optical hollow-core microstructured bandgap fiber is shown in Fig. 5(a).

As is well known from optics, these microstructure waveguides suffer from high-confinement losses due to the finite number of air holes composing the cladding lattice [97,98] and scattering loss due surface roughness at the dielectric–air interface [99]. The leakage can be suppressed by incorporating sufficient concentric rings of air holes around the core or by increasing the ratio of cladding air-hole diameter to hole-to-hole spacing pitch (d/Λ). However, the higher the number of concentric air-hole rings, the more difficult the process of fabrication becomes. The scattering losses, which are inversely proportional to the operating wavelength, can be suppressed to a certain degree by controlling the fiber fabrication parameters.

The concept of hollow-core microstructured bandgap fibers has been expanded to THz frequencies [98,100–102]. The advantages of using these fibers for guiding THz are the following: first, like all other hollow-core fibers, most of the electromagnetic field propagates predominantly in the air core (which is a transparent medium for THz); and second, at THz frequencies (longer wavelength compared to invisible and optics), scattering losses are low and

Figure 5



(a) Scanning electron microscope image of optical photonic bandgap fiber [96]. Published by courtesy of Jonathan Knight. (b) Concentric cylindrically periodic Bragg fiber with a large variation in index between the cladding layers. (c) Microscope image of a ring-structured Bragg fiber. Reproduced with permission, ©2008. Optical Society of America [39]. In contrast to omnidirectional Bragg fiber, the ring-structured Bragg fiber is made up of a single material, and variation in index between the cladding layers is achieved by including alternating circular rings of air holes. (d) Cob/spider-web structured Bragg fiber. These Bragg fibers are also made up of single material (concentric layers of material and air), and struts are used to keep the structure together.

do not significantly affect the overall loss mechanism [103]. It has been shown that just three concentric rings of air holes in the cladding were enough for a THz hollow-core microstructured bandgap fiber to have negligible leakage loss (0.0002 cm^{-1}) compared with cladding material absorption loss (0.01 cm^{-1}) [102].

A specific type of hollow-core microstructured bandgap waveguide is Bragg fiber. The multilayer dielectric bandgap waveguide, well known as Bragg fiber in optics, consists of a hollow core surrounded with a concentric cylindrically periodic (CP) structure [74,77,78]. So far at the optical regime, there are three types of hollow-core Bragg fibers. The first one is the omnidirectional Bragg fiber, made up of a combination of either glass or polymer materials with very large index variation between concentric cladding layers, as shown in Fig. 5(b). The second type is ring-structured Bragg fibers, made up of a single material with alternating circular rings of air holes, which behave like the low-index layers of an omnidirectional Bragg fiber, as shown in Fig. 5(c). Finally, the third type is the cob/spider-web structured Bragg fiber made up of layers of single material and air, where a certain number of supporting strips, called struts, are used to keep the structure together, as shown in Fig. 5(d). All three types of Bragg fibers have also been explored for guiding THz radiation [39,104,105].

A hollow-core multilayer bandgap waveguide featuring concentric CP layers (PVDF and PC polymers) was theoretically studied for THz guidance in 2007 [104]. Theoretical loss values less than 0.02 cm^{-1} for $1 < \omega < 3 \text{ THz}$ were predicted for a 1 mm core diameter. Following this theoretical report, another hollow-core bandgap waveguide made of single material (i.e., spider-web structured bandgap waveguides) was also theoretically studied and reported for THz guidance in 2007 [105]. Absorption losses less than $1.8 \times 10^{-5} \text{ cm}^{-1}$ in the frequency range 1.5–4.3 THz were theoretically calculated for a 16 mm core diameter. The loss reported for the spider-web structured bandgap waveguide is much lower than that of the multilayer bandgap waveguide due to large air-core diameter. The propagation losses in Bragg fibers are scaled according to $f^{-2}d_{\text{core}}^{-3}$, where d_{core} is the diameter of the core and f is the frequency of the confined light [106]. Direct scaling up of the optical dimensions results in large THz waveguide dimensions (6–10 mm), making it potentially very inflexible. The structure also suffers from high losses, especially at bends or discontinuities, due to coupling of the propagating mode TE_{01} to the lossy TM_{11} degenerate mode. Degenerate modes are modes that have identical cut-off frequency, e.g., TE_{0n} and TM_{1n} in circular cross-section waveguides.

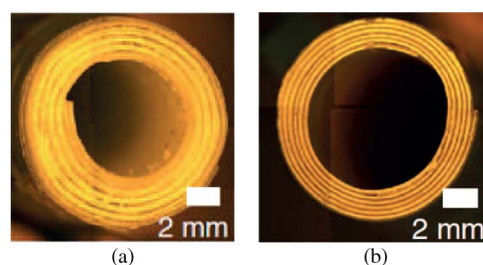
For a hollow-core multilayer bandgap waveguide, it is difficult to find two materials that have larger index contrast (the relative size of the bandgap is proportional to the relative index contrast), similar thermal and mechanical properties, and compatible processing techniques in realizing the structure. Therefore, guiding of THz pulses in the hollow-core Bragg waveguides was first observed in a single-material (PMMA) Bragg waveguide, shown in Fig. 5(c) [39]. The pre-forms were prepared by drilling the hole pattern into a PMMA rod and were later drawn down to 5–6 mm diameter waveguides. The minimum absorption loss of the pulse guided in the hollow core was estimated to be 0.44 cm^{-1} at 1.0 THz and 0.2 cm^{-1} at 1.3 THz from the experimental measurements. An n-type bulk indium-arsenide (InAs) emitter and a photoconductive antenna were used for the generation and detection of THz radiation. Parabolic mirrors were used to couple into and out of the waveguide (options B and E shown in Fig. 1).

In 2011, two other types of ring-structured Bragg waveguides (air–polymer layers and two polymer material layers) were fabricated and experimentally characterized [106]. The ring-structured waveguides were fabricated by rolling up a thin film with a layer of powder on top to create the air gap between the layers, shown in Fig. 6(a), or by rolling up a bilayer of thin films, shown in Fig. 6(b). The film layers used were polymer (PE) and a doped-polymer (TiO_2 particles in PE). Parabolic mirrors were used to couple into and out of the waveguide (options B and E shown in Fig. 1). Both waveguides were estimated to have propagation losses less than 0.05 cm^{-1} around 0.82 THz (air–polymer bilayer) and 0.69 THz (two polymer bilayer).

In general, the microstructured bandgap waveguides allow low-loss propagation of THz pulses in the bandgap regime, which is narrow compared to the broad spectrum of THz. The operational bandwidth of these waveguides is defined by the bandgap width. Although they can be tuned to operate in a different frequency band, their bandwidths are narrow compared to the broad THz spectrum. The loss and dispersion of these waveguides increases as the frequency approaches the edges of the bands. Moreover, they have large diameters, which makes the waveguides inflexible and not proper guiding structures for integrated THz devices. Additionally, these fibers suffer from multimode propagation due to their large core size.

Kagomé hollow-core microstructured waveguides. The guiding mechanism in Kagomé hollow-core microstructured waveguides is via the formation Von-Neumann Wigner quasi-bound states within a continuum [73,79,80,107,108]. The cladding of these waveguides does not support photonic bandgaps. The core-guided modes cohabit with those of the cladding modes without notable interaction. In other words, the guided modes confined in the hollow core are prevented from efficiently coupling to the cladding due to the antiresonance effect of the Kagomé lattice. Figure 7(a) shows an example of a Kagomé-lattice optical fiber. Kagomé-lattice waveguides offer a wider transmission band compared to Bragg waveguides (≈ 3 larger bandwidth) [109]. However, the absorption (material) losses of Kagomé-lattice waveguides are higher than those of Bragg waveguides (≈ 8 times higher). Similar to Bragg waveguides, the leakage loss for Kagomé-lattice waveguides (even with one ring of tubes as cladding) is negligible compared to absorption loss, except where the frequencies coincide with cut-off frequencies.

Figure 6



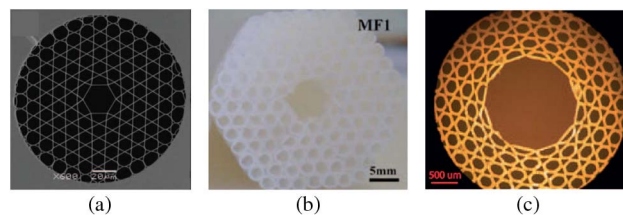
Cross section of Bragg fibers: (a) spider-web Bragg fiber (air–polymer) and (b) concentric Bragg fiber (polymer-doped polymer). Reprinted with permission from L. Vincetti, *Microwave Opt. Technol. Lett.* 51, 1711–1714 (2009) [102]. Copyright 2009, John Wiley and Sons.

The hollow-core microstructured fiber proposed by Lu *et al.* [69] is the first example of a Kagomé-lattice optical fiber adapted for guiding THz radiation. This hollow-core microstructured fiber was composed of a central hollow core and a cladding layer formed by periodic arrangements of Teflon tubes, as shown in Fig. 7(b). The attained structure was suitable for the guidance of THz pulses, and no further steps (drawing) were required. A low attenuation constant less than 0.01 cm^{-1} was experimentally achieved at 0.770 THz, which was more than 100 times lower than the bulk material. It has been shown that the absorption losses of the proposed fiber are dominated by the first cladding layer, and the increase of the ring number has little influence on the modal properties of the waveguides. Theoretical investigations of these waveguides reveal that the transmission spectrum exhibits an alternation of low- and high-loss bands. The minimum loss in each low-loss region depends on the tube diameter, while the frequency ranges of low loss and dispersion depend on the thickness of the tubes [108,111]. Increasing the tube diameter reduces the minimum loss by about one order of magnitude, flattens the dispersion, and increases the core and total diameter of the waveguide. Meanwhile, decreasing the thickness of the tubes leads to a wider transmission band.

A Kagomé hollow-core microstructured fiber made of PMMA tubes was also reported for guiding THz radiation [110]. Unlike the previous Kagomé waveguide, the preform was drawn down to 5–6.8 mm outer diameters (core diameters of 1.6–2.2 mm, respectively), as shown in Fig. 7(c). The average attenuation constant 0.6 cm^{-1} is experimentally reported over 0.65–1.0 THz, which is on average 20 times lower than the bulk material. Photoconductive switches with the arrangement shown in options A and D in Fig. 1 were used for generation and detection of THz pulses.

A drawback of Kagomé waveguides is that they have diameters of the order of a few tens of millimeters [108,111]. As an example for the seven ring microstructure fiber [69], the total fiber diameter ranges from 18 to 35 mm. It should be noted that the diameter of the fiber is greater than 10 mm even when a single layer of cladding is used. Thus, these waveguides are not flexible. Another disadvantage of these fibers is that they are multimode due to the large core diameters. It has been shown that reducing the core size leads to single-mode propagation at the expense of high fundamental mode propagation losses and dispersion. It should be noted that single-mode propagation can be obtained

Figure 7



- (a) Scanning electron microscope image of the optical Kagomé fiber. Reproduced with permission, ©2006. Optical Society of America [79]. (b) THz hollow-core microstructured fiber. Reprinted with permission from J.-Y. Lu, Appl. Phys. Lett. 92, 064105 (2008) [69]. Copyright [2008] American Institute of Physics LLC. (c) Optical micrograph of PMMA Kagomé fiber. Reproduced with permission, ©2011. Optical Society of America [110].

to some extent by controlling the launch condition [112]. A third disadvantage of these waveguides is that the loss and dispersion curves contain irregular small perturbations in the low-loss regions (within the transmission band) due to the weak coupling between core modes and cladding modes [108].

An advantage of hollow-core waveguides is that the THz pulses propagate predominantly in the hollow core with only a small fraction propagating in the material, resulting in low absorption losses. These waveguides can be tailored to offer low loss and dispersion in the required transmission band. Another advantage of these waveguides is that they are suitable for sensing applications; i.e., the sample under test can be located in the core where a better interaction of the field and sample can occur compared to free-space propagation systems.

In spite of the above advantages, generally the hollow-core waveguides have transmission windows by virtue of the resonance or bandgap effects. Therefore, they only offer low loss and dispersion for the designed narrow window and are not suitable to guide the broad THz spectrum. Another drawback of these waveguides is that their dimension is in the order of a few millimeters. Thus, they are usually inflexible. Reducing the core diameter leads to an increase in the absorption loss. A summary of the key parameters of these hollow-core waveguides is presented in Table 3.

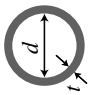
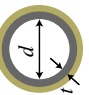
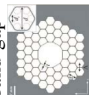

A feasible approach to reduce the air-core dimension of hollow-core waveguides and consequently achieve flexible THz waveguides is the exploitation of metamaterials, man-made artificial materials [113]. Theoretical studies have shown that hollow-core waveguides with metamaterial cladding can guide modes even when the core diameter is more than 10 times smaller than the operating wavelength [114–116]. Such waveguides, if fabricated, not only will have the advantage of guiding THz radiation in the air core but also will be flexible.

4.2. Solid-Core Waveguides/Fibers

The electromagnetic waves are guided based on well-known total internal reflection in solid-core waveguides/fibers, where the effective refractive index of the core is higher than that of the cladding. Here, we have divided solid-core waveguides into three types: waveguides with air-cladding (microwires), waveguides with microstructured cladding, and waveguides with single air-hole discontinuity in the core.


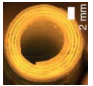
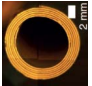

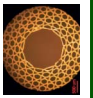
Microwire (air-clad dielectric waveguides). Sapphire fiber [117] and the plastic ribbon waveguide [118] were the first two dielectric waveguides proposed by the Oklahoma State University research group. As the names indicate, these structures were made, respectively, of sapphire with diameters of

Table 3. Summary of THz Hollow-Core Dielectric Waveguides^{a,b,c,d,e}

Waveguide	Dimensions	Material	α_{eff} [cm ⁻¹]	Remarks	Refs.
 <p>Single clad</p>	$d = 8$ mm, $t = 0.12$ mm, $l = 30$ cm	PVDF	0.015 (ave) ($1 < f < 2$ THz)	Loss 3 times lower than Ni-Cu pipe.	[87]
	$d = 9$ mm, $t = 0.5$ mm, $l = 3$ m	Teflon	< 0.02 ($0.34 < f < 0.53$ THz) $\approx 8 \times 10^{-4}$ $f = 0.4$ THz	Mode: HE ₁₁ . 200–300 GHz bandwidth.	[40]
 <p>Hybrid clad</p>	$t = 10$ μ m, $d = 2.2$ cm, $l = 30$ 90 cm	Ag/PS coated	< 0.002 $f = 2.5$ THz	Mode: TE ₀₁ or TE ₁₁ ; thickness of the coating determines the lowest loss mode.	[119]
	$t = 26$ μ m, $d = 3$ mm, $l = 30$ & 100 cm	Ag/PE coated	$< 4 \times 10^{-3}$ ($1.2 < f < 2$ THz) $\approx 3.2 \times 10^{-3}$ $f = 1.5$ THz	3 dB lower than Ag pipe.	[92]
 <p>Microstructured band-gap</p>	$\Lambda = 900$ μ m, $d = 882$ μ m, $t = 9$ μ m, $R_c = 2.7$ mm	Teflon HDPE	< 0.01 ($0.895 < f < 1.145$ THz) ≈ 0.005 $f = 1$ THz < 0.01 ($0.82 < f < 1.02$ THz) ≈ 0.0035 $f = 1$ THz	Only theoretical results reported. Mode: HE ₁₁ (multimode). Dispersion: < 2 ps/nm/km. Confinement loss: 0.1 dB/m narrow transmission bandwidth.	[102]
 <p>Bragg</p>	$D_{core} = 1$ mm, $l = 1$ m 31 layers of PVD/PC t of each layer ≈ 50 μ m	PVDF & PC	< 0.02 ($1 < \omega < 3$ THz)	Only theoretical results reported. Mode: HE ₁₁ (TEM). Different guiding mechanisms.	[104]
	$D_{core} = 16, 20$ & 30 mm, $d_{air} = 0.5, 0.7$ & 2.25 mm, $d_{material} = 25, 70$ & 150 μ m, $l = 28$ cm	HDPE	$< 2 \times 10^{-5}$ ($0.3 < f < 4.3$ THz) $\approx 2 \times 10^{-6}$ $f = 3.34$ THz	Only theoretical results reported. Mode: TE ₀₁ . The frequency range is covered by three different waveguides.	[105]

(Table continues.)

Table 3. Continued

Waveguide	Dimensions	Material	α_{eff} [cm ⁻¹]	Remarks	Refs.
	$D_{\text{core}} = 670 \text{ }\mu\text{m}$, $l < 1.5 \text{ cm}$ $D_{\text{fiber}} = 6.3 \text{ \& } 5.6 \text{ mm}$	PMMA	1.3 (ave) ($0.8 < f < 1.4 \text{ THz}$) $\approx 0.4 f = 1 \text{ THz}$ 1.1 (ave) ($1 < f < 1.6 \text{ THz}$) $\approx 0.2 f = 1.3 \text{ THz}$	Mode: HE ₁₁ (TEM). Ave: average loss values. THz radiation propagates both in the core and in the cladding.	[39]
	$D_{\text{core}} = 6.73 \text{ mm}$, $l = 21.4 \text{ cm}$ 10 layers of $d_{\text{air}} = 150 \text{ }\mu\text{m}$, $d_{\text{material}} = 254 \text{ }\mu\text{m}$	PTFE	< 0.3 ($0.1 < f < 2 \text{ THz}$) $\approx 0.028 f = 0.82 \text{ THz}$	Lower mode (HE ₁₁) losses compared to doped PE Bragg. Multimode propagation.	[106]
	$D_{\text{core}} = 6.33 \text{ mm}$, $l = 22.5 \text{ cm}$ 12 layers of $d_{\text{mat1}} = 100 \text{ }\mu\text{m}$, $d_{\text{mat2}} = 135 \text{ }\mu\text{m}$	PE & TiO ₂ doped PE	< 0.3 ($0.1 < f < 2 \text{ THz}$) $\approx 0.042 f = 0.69 \text{ THz}$	Less clear transmission window compared to air-PE Bragg. Multimode propagation.	[106]
Kagomé 	$D_{\text{core}} = 5.5 \text{ mm}$, $l = 20 \text{ cm}$, tubes In/out diameters: 1.68/2.08 mm	Teflon tubes	< 0.01 ($f = 0.77 \text{ THz}$)	Mode: HE ₁₁ (multimode). $d \propto$ minimum loss. $l \propto$ bandwidth	[69] [108]
	$D_{\text{core}} = 6.33 \text{ mm}$, $l = 15 \text{ \& } 45 \text{ mm}$ 12 layers of $d_{\text{core}} = 1.6 \text{ \& } 2.2 \text{ mm}$, $d_{\text{fiber}} = 5 \text{ \& } 6.8 \text{ mm}$	PMMA	0.6 (ave) ($0.65 < f < 1 \text{ THz}$)	Mode loss ≈ 20 times less than clad-PMMA loss. Ave: average loss values.	[110]

^a The third image is reprinted with permission from L. Vincetti, Microwave Opt. Technol. Lett. **51**, 1711–1714 (2009) [102]. Copyright 2009, John Wiley and Sons.
^b The sixth image is reproduced with permission, ©2008. Optical Society of America [39].
^c The seventh and eighth images are reproduced with permission, ©2011. Optical Society of America [106].
^d The ninth image is reprinted with permission from C.-K. Sun, Appl. Phys. Lett. **92**, 064105 (2008), American Institute of Physics LLC.
^e The tenth image is reproduced with permission, ©2011. Optical Society of America [110].

150–325 μm and HDPE slabs with thicknesses of 120–150 μm . The structures offer lower absorption loss than the bulk material loss. This occurs by virtue of the subwavelength dimension of the waveguides, where the propagating mode is not tightly confined to the waveguide material and expands to the air. Losses less than 6 cm^{-1} for $f < 2.5\text{ THz}$ and losses less than 1 cm^{-1} for $0.1 < f < 3.5\text{ THz}$ were reported for sapphire fiber and ribbon waveguide, respectively. The absorption losses of these waveguides were much lower than those of coplanar waveguides discussed in Subsection 1.1. Nevertheless, the achieved losses were not comparable to those of the parallel-plate metallic waveguide and the bare metal wire and hollow-core dielectric waveguides discussed above.

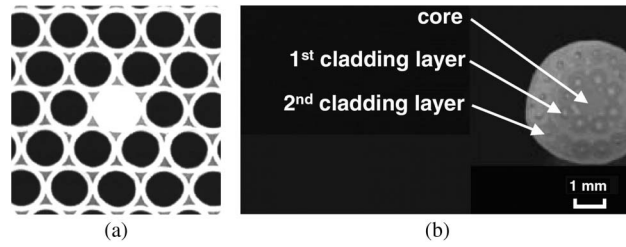
In 2006, Chen *et al.* [38] from Taiwan University reported loss values less than 0.01 cm^{-1} near 0.3 THz (1 mm wavelength) in a polyethylene (PE) subwavelength air-clad waveguide. An air-clad waveguide with a core diameter of 200 μm is used to transfer THz radiation. Compared to the sapphire waveguide proposed earlier in the literature, this waveguide has different hosting material and is only analyzed at low frequencies where the waveguide dimension is more than four times smaller than the operating wavelengths (830–970 μm). The subwavelength dimension pushes a large portion of the power transmitted by the structure into the air-clad waveguide, which is transparent for THz frequencies, leaving a small portion of it in the low-loss plastic material. Therefore, the loss averaged in the transverse plane reduces dramatically. The concept used by Chen *et al.* [38] is similar to the concept developed in optics, i.e., optical nanowires [120]. Since the enhanced evanescent field behavior occurs for micrometer diameter fibers in the T-ray band, these waveguides are also known as *microwires* in the THz spectrum [2,121,122].

Subwavelength air-clad waveguides are flexible due to their subwavelength dimension (a few hundred micrometers). The extension of the propagating mode into the air allows coupling via surface contact and straightforward interaction of the mode with the surrounding environment, leading to practical applications in sensing. For example, these waveguides have been utilized as straight THz sensor tips for spectroscopy [123,124], THz directional couplers [125], and waveguide-based THz endoscopes in interferometric imaging [126].

In spite of that, a disadvantage of these subwavelength air-clad waveguides is that they suffer from high losses due to any perturbation (e.g., bends) to the structure. This occurs due to the weak confinement of the mode to the waveguide compared to waveguides with strong confinement of the field in the core (e.g., conventional core/clad fibers and hollow-core bandgap waveguides). Moreover, special handling is required for such waveguides with extended field since any small perturbation leads to high losses. Suspended core fibers (where a second layer of cladding is considered in which the extended field is almost zero) have been proposed in optics to facilitate handling and practicality. This concept has also been transferred to THz microwires [127].

Solid-core microstructured waveguide. The guiding mechanism of solid-core microstructured waveguides, also known as solid-core photonic crystal fiber (PCF), is achieved by total internal reflection, while in PFCs with low-index cores, e.g., air cores, it is achieved by the photonic bandgap effect. Han *et al.* [70] were the first to realize, fabricate, and experimentally demonstrate the loss and dispersion of solid-core microstructured waveguides in the THz spectrum. As shown in Fig. 8(a), the structure is fabricated from HDPE tubes and a

Figure 8



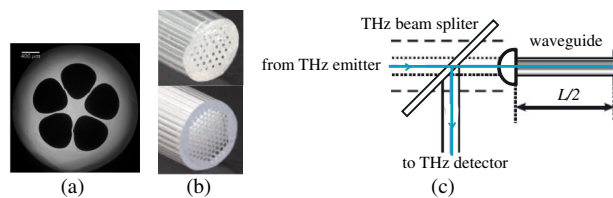
(a) Optical micrograph of a solid-core photonic crystal fiber. Reprinted with permission from H. Han, Appl. Phys. Lett. 80, 2634–2636 (2002) [70]. Copyright [2002] American Institute of Physics LLC. (b) Photograph of the cross section of a Teflon solid-core photonic crystal fiber [128]. Copyright 2004 The Japan Society of Applied Physics.

filament that represent, respectively, the cladding and the core. Relatively low loss (less than 0.5 cm^{-1}) and low dispersion (average group velocity of 2 ps/THz/cm at 0.4 THz) were attained within the bandwidth of $0.1\text{--}3 \text{ THz}$ [70].

The attenuation of a guided mode of the solid-core microstructured waveguides depends on the field confinement in the core and the core material absorption. It has been shown that the main contribution of the transmission loss is the material absorption loss [70]. Consequently, the attenuation can be reduced by using a material with lower loss in the THz regime. Goto *et al.* [128] have demonstrated that fabricating a similar solid-core PCF from polytetrafluorethylene, commonly known as Teflon, reduces the solid-core PCF loss further to less than 0.12 cm^{-1} for $0.1\text{--}1.3 \text{ THz}$. This is due to a relatively low refractive index of Teflon ($n = 1.46$) compared to that of HDPE ($n = 1.53$) [129], which leads to lower confinement of THz radiation into the solid core and consequently lower loss.

The loss of solid-core microstructured waveguides was further improved by using COC, commercially known as TOPAS and Zeonex, as the host material [50,130]. Losses as low as 0.1 cm^{-1} for $0.35\text{--}0.65 \text{ THz}$ are reported for COC fibers, almost identical to the bulk material loss of COC. Photographs of different solid-core microstructured waveguides fabricated from COC are shown in Figs. 9(a) and 9(b). These COC waveguides have s-shaped dispersion curves with absolute dispersion values less than 1 ps/THz/cm for $0.4\text{--}1.4 \text{ THz}$ and zero dispersion between 0.4 and 0.6 THz .

Figure 9



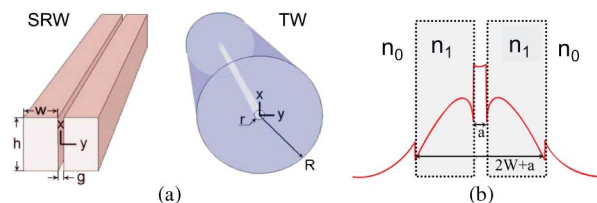
Photographs of two different solid-core photonic crystal fibers fabricated from COC. (a) Reproduced with permission, ©2011. Optical Society of America [130]. (b) Reproduced with permission, ©2009. Optical Society of America [50]. (c) Reflection arrangement considered for constant in- and out-coupling of the THz signal during loss measurements. Reproduced with permission, ©2009. Optical Society of America [50].

Unlike the transmission mode characterization setups employed for waveguides discussed so far, the COC microstructured waveguide in [50] was characterized in a reflection mode THz TDS system. In order to have a constant in- and out-coupling of the THz pulses during loss measurements, a reflection arrangement is considered as shown in Fig. 9(c). A metallic reflector is positioned at the back end facet of the waveguide for this purpose, and the waveguide is also cleaved from this end for loss measurements. Two photoconductive antennas were used for generation and detection of broadband THz pulses. A COC beam splitter is used to separate the reflected THz beam from the incoming beam. A COC hyper-hemispherical lens is employed for coupling in and out of the solid-core microstructured waveguide.

Compared to air-core microstructured waveguides, the solid-core microstructured waveguides have a broader transition bandwidth since the guiding mechanism in them is based on total internal reflection and not on antiresonance or bandgap effects. Thus these waveguides are better suited for broadband THz guidance. Although the TOPAS solid-core microstructured waveguides can be bent (90° bend) by heating the waveguide, generally they are rigid due to their large dimension (a few millimeters).

Waveguides with a low-index discontinuity in the core. Nagel *et al.* [53] have proposed low-index discontinuity waveguides in order to improve the confinement of the THz radiation, compared to that of an air-clad waveguide, as shown in Fig. 10(a). In that work, Nagel *et al.* [53] transferred the concept proposed by Almeida *et al.* [10] for integrated optical devices to the THz range. Almeida *et al.* [10] have shown theoretically and experimentally that a high-index dielectric single-mode rectangular waveguide with a slit along the axis of wave propagation enhances and confines a substantial fraction of power in the low-index split region as shown in Fig. 10(b). At any interface between two materials with no surface charge, since the normal components of the electric displacement field are continuous, there is a discontinuity in the electric-field strength; i.e., the electric field enhances on the low refractive index side. The strength of the enhanced electric field depends on the square of the ratio of refractive indices and the electric-field strength at the high-index side. As a result, a higher enhanced electric field is formed at a low-index discontinuity interface, if it is introduced within a region of a waveguide structure where the electric field is originally stronger than the other regions. The enhanced electric field at the low-index side of any discontinuity rapidly decays away from the interface discontinuity. However, if the dimension of the low-index discontinuity is at the subwavelength scale, the decay of the evanescent field within the

Figure 10



(a) Geometries of a slot rectangular waveguide (SRW) and a tube waveguide (TW). Reproduced with permission, ©2006. Optical Society of America [53]. (b) Electric-field enhancement within low-index discontinuity.

discontinuity is minimal. Thus a localized intensity enhancement can be achieved throughout the discontinuity region [11,131]. The concept has been expanded to THz by Nagel *et al.* [53], and the attenuation, dispersion, and single-mode confinement properties for two structures, a split rectangular waveguide and a tube waveguide shown in Fig. 10(a), were investigated. The mode confinement in the virtually lossless low-index air gap reduces THz transmission losses compared to that of the same structure without the split and increases the confinement of the mode compared to bare metal wires [53].

For a tube waveguide composed of fused silica, loss values less than 0.7 cm^{-1} are measured for the frequency range of 0.4–0.6 THz [53]. The measured effective permeability ($\epsilon_{\text{eff}} = n_{\text{eff}}^2$) for the tube waveguide varies from 2 to 4 over the frequency range of 0.3–0.7 THz. The numerically calculated loss and effective relative permittivity of a slot rectangular waveguide made of high-resistivity silicon are less than 0.01 cm^{-1} and 2, respectively, for 0.5–0.9 THz. For characterization of the tube waveguide, two identical photoconductive antennas embedded in a parallel-plate waveguide are used for the generation and detection of broadband THz radiation. The parallel-plate waveguide serves as the output and input port of the emitter and detector [14,53].

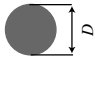

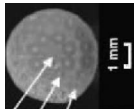
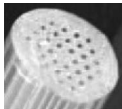
4.3. Porous-Core Waveguides

To improve the effective loss (also known as effective material loss) and confinement simultaneously, a class of waveguides, known as *porous fiber*, was proposed independently by two research groups [132–134]. Porous-core waveguides, porous fibers, are created by including a distribution of subwavelength air holes within the *core* of an air-clad fiber. The guiding mechanism in these waveguides is based on total internal reflection. A typical example of porous fiber is shown in Fig. 11(a). The distribution, shape, and size of the holes determine the porosity of the structure, which is defined as the fraction of the air holes to the core area. In the early days of THz porous fibers, only circular air holes were considered [132–134]. However, other geometries can also be introduced into the core of these fibers [43,135–137].

The guiding mechanism in solid-core dielectric waveguides is based on total internal reflection. These waveguides suffer from material absorption losses. This loss can be reduced if the dimension of the core is chosen smaller than the operating wavelengths, since a higher portion of the mode power propagates in the air-clad with almost zero loss. However, this reduces the confinement of the mode to the waveguide. A method for increasing the confinement was to introduce a subwavelength discontinuity in the waveguide. The absorption loss in this waveguide is directly proportional to the bulk material absorption of the hosting material. Therefore, the absorption losses of the waveguides can be minimized when low-loss dielectric materials such as COC are used. However, these waveguides are rigid due to their dimension.

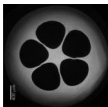
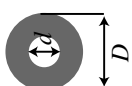
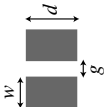
A summary of all the key parameters discussed for the above hollow-core waveguides is presented in Table 4.

Table 4. Summary of THz Solid-Core Dielectric Waveguides^{a,b,c,d}

Waveguide	Dimensions	Material	α_{eff} [cm ⁻¹]	Dispersion	Remarks	Refs.
	$D = 150, 250, \text{ \& } 325 \text{ }\mu\text{m}$, $l = 7.3, 7.8 \text{ \& } 8.3 \text{ mm}$	Sapphire	<6 ($f' < 2.5 \text{ THz}$)	$0.6 \text{ ps} \rightarrow 10\text{--}13 \text{ ps}$	Mode: HE ₁₁	[118]
	$D = 200 \text{ }\mu\text{m}$, $l = 6, 13, 17.5 \text{ cm}$	PE	<0.01 ($0.35 < f < 0.35 \text{ THz}$)	No value reported	Different regimes of guidance in the transmission band.	[38]
	$b = 150 \text{ \& } 120 \text{ }\mu\text{m}$, $a = 2 \text{ cm}$, $l = 10 \text{ \& } 20 \text{ mm}$	HDPE	<1 ($0.1 < f < 3.5 \text{ THz}$)	$1 \text{ ps} \rightarrow 20, 40 \text{ ps}$	Mode: TM ₀	[119]
	$D_{\text{core}} = 500 \text{ }\mu\text{m}$, tubes in/out diameters: $0.5/0.55 \text{ mm}$, $l = 2 \text{ cm}$	HDPE	<0.5 ($0.1 < f < 3 \text{ THz}$) ≈ 0.2 ($f = 1 \text{ THz}$)	$0.8 \text{ ps} \rightarrow 5 \text{ ps}$ ≈ 14 ($f = 0.25 \text{ THz}$) ≈ 2 ($f = 0.4 \text{ THz}$) ≈ 0 ($f = 0.5 \text{ THz}$) ≈ -0.3 ($f > 0.6 \text{ THz}$)	Mode: HE ₁₁ . Dispersions are in ps/THz/cm.	[70]
	$D_{\text{core}} = 1 \text{ mm}$, tubes in/out diameters: $0.25/0.75 \text{ mm}$, $l = 5, 10, \text{ \& } 15 \text{ cm}$	Teflon	<0.12 ($0.1 < f < 1.3 \text{ THz}$)	No value reported	Mode: HE ₁₁ . Knife-edge measurements to test the confinement of THz radiation.	[128]
	$D_{\text{hole}} = 250 \text{ }\mu\text{m}$, $\Lambda = 560 \text{ }\mu\text{m}$, $l = 29 \text{ mm}$	COC	<0.1 ($0.35 < f < 0.65 \text{ THz}$) ≈ 0.02 ($f = 0.6 \text{ THz}$)	<1 ($0.4 < f < 1.4 \text{ THz}$) ≈ 0 ($0.5 < f < 0.6 \text{ THz}$)	Mode: HE ₁₁ . Dispersion parameters β_2 are in ps/THz/cm.	[50]

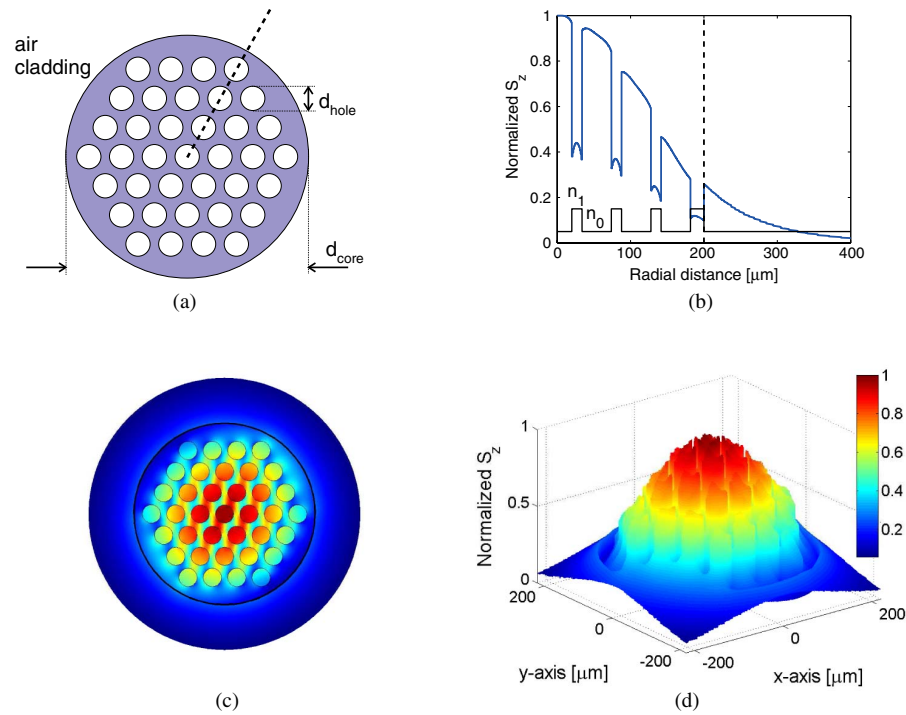
(Table continues.)

Table 4. Continued

Waveguide	Dimensions	Material	α_{eff} [cm^{-1}]	Dispersion	Remarks	Refs.
	$D_{\text{core}} = 400$ μm , $D_{\text{fiber}} = 3$ – 4 mm, $l = 20$ – 70 mm	COC	< 0.3 ($0.2 < f < 1$ THz)	< 1 ($0.4 < f < 1.2$ THz) ≈ 0 (0.7 THz)	Mode loss (HE_{11}) equal to material loss dispersion parameter β_2 is in ps/THz/cm.	[130]
Low index discontinuity 	$D = 181.5$ μm , $d = 27$ μm , $l = 30$ & 40 mm	Silica	< 0.7 ($0.4 < f < 0.6$ THz)	$2 < \epsilon_{\text{eff}} < 4$ ($0.3 < f < 0.7$ THz)	Mode: HE_{11}	[53]
	$g = 15$ μm , $w = 45$ μm , $h = 75$ μm	High-resistivity silicon	< 0.01 ($0.5 < f < 0.9$ THz)	$1 < \epsilon_{\text{eff}} < 2$ ($0.5 < f < 0.9$ THz)	Mode: quasi TE (analogous to TM mode in slab waveguides). Only theoretical results reported.	[53]

^a The third image is reprinted with permission from H. Han, Appl. Phys. Lett. **80**, 2634–2636 (2002) [70]. Copyright [2002] American Institute of Physics LLC.
^b The fourth image is reproduced with permission, Copyright 2004 The Japan Society of Applied Physics [128].
^c The fifth image is reproduced with permission, ©2009. Optical Society of America [50].
^d The sixth image is reproduced with permission, ©2011. Optical Society of America [130].

Figure 11



Power profile distribution of a porous fiber with holes on a triangular lattice: (a) Cross section and geometrical definitions of the triangular lattice porous fiber. (b) Normalized z -component of the Poynting vector, S_z , profile along the dashed line shown in (a), of the fundamental mode of a polymer porous fiber with core radius of $d_{\text{core}}/2 = 200 \mu\text{m}$, hole radii of $d_{\text{hole}}/2 = 20 \mu\text{m}$, and 37% porosity at $f = 0.5 \text{ THz}$ ($\lambda = 600 \mu\text{m}$). The vertical dashed line represents the core to cladding interface, and the lower solid line represents the refractive index profile. (c) 2D and (d) 3D view of the normalized S_z of the porous fiber. Note that S_z is normalized by its maximum and the color bar shows the normalized S_z . Reproduced with permission, ©2008. Optical Society of America [134].

These porous fibers offer lower material losses compared to a similar diameter of subwavelength air-clad waveguides (microwires) by virtue of less material residing in the core. This concept has been used in the optical regime; i.e., elongated void regions have previously been used in photonic crystals to improve the transmission efficiency simply by reducing the material [138]. This is not the only benefit of having subwavelength air holes within the core. It has been shown that for similar diameter, porous fiber offers better confinement and consequently lower bending losses [134]. Moreover, it has been shown that for similar loss values, porous fibers enable reduced distortion (frequency dependent loss and dispersion) of a broadband THz pulse compared to microwires [43]. It has also been demonstrated that introducing asymmetrical subwavelength air holes in the core of porous fibers leads to modal birefringence [135]. Modal birefringence arises from effective refractive index differences between x - and y -polarization modes, $|n_x - n_y|$. The porous fiber modal birefringence ≈ 0.026 [135] is comparable to achieved high birefringence of ≈ 0.021 at 0.3 THz [71] in THz solid-core microstructured fibers, and ≈ 0.025 at 1550 nm [139]

in photonic crystal fibers. It is almost an order of magnitude higher than the birefringence of ≈ 0.001 at 1 THz [101] in THz air-core microstructured Bragg fibers.

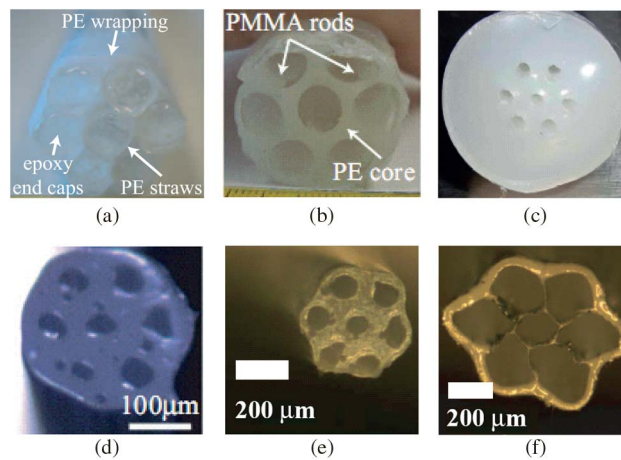
All the above benefits occur due to the field enhancement within subwavelength air holes. The concept of field enhancement within low-index discontinuity (as explained above) is demonstrated in Fig. 11(b), which shows the normalized z -component of the Poynting vector ($S_z = (1/2)\vec{E} \times \vec{H} \cdot \hat{z}$) profile of the fundamental mode of the porous fiber along the arrow shown in Fig. 11(a). The normal component of the electric field and as a result the power intensity (S_z) are enhanced at each air–material interface and stay localized in the subwavelength air holes, where the refractive index is n_0 . This phenomenon occurs for all the subwavelength air holes in the structure, as can be seen in Fig. 11(c). Since the enhancement coefficient of the normal component of the electric field at each interface is constant, n_1^2 , the intensity of the localized power intensity (S_z) depends on the location of the subwavelength air-hole position. The closer the subwavelength air hole to the center of the fiber, where the electric-field intensity is stronger, the stronger the localized power intensity. Therefore the envelope of the intensified profile of the power has a profile pattern similar to that of the air-clad fiber without subwavelength holes. For the chosen porous fiber dimensions, the power profile envelope has a Gaussian shape, as shown in Fig. 11(d).

To reduce the effective material loss in a porous fiber, one needs to be able to access high porosity values. Design and fabrication of waveguides with air-clad and high porosity ratio in the core are challenging; however, the techniques used for fabrication of MOFs pave the path for the fabrication of THz porous waveguides. These porous-core waveguides with subwavelength dimension and features require a two-stage process discussed earlier: a preform fabrication and drawing process. Different preform fabrication techniques have been proposed for fabrication of these waveguides: stacking of capillary tubes, casting into a mold, drilling the hole pattern, and the extrusion technique.

To fabricate preforms through the stacking technique [140], the capillary tubes were arranged in a two-dimensional triangular lattice, as shown in Fig. 12(a), and were drawn using self-pressurization. For this purpose, first one end of the fiber was sealed off, e.g., epoxy glue in this case, and then drawn to fiber. Trapping of air within the holes allows the pressure of the holes to build up and prevents hole closure during the drawing process. However, partial hole closure cannot be prevented unless active pressurization, in which the holes are pressurized utilizing a controlled gas source, is used. The cross section of resultant porous fiber is shown in Fig. 12(d). A drawback of the approach is that the hole closure possibility is very high and the maximum achieved porosity so far is 8%–18% [140]. Moreover, this method is only suitable for fabrication of porous fiber with a hexagonal array of circular air holes.

Another technique employed for fabrication of porous fibers utilizes casting of the preform into a structured mold. Two different approaches were considered for this purpose [141]. In the first approach, a composite preform is built by casting the desired material, in this case PE, into a mold with polymer rods, in this case PMMA, as shown in Fig. 12(b). The composite solid preform was pulled into fiber where the presence of PMMA rods prevents hole closure during the drawing process. Afterwards, the fiber segments were submerged into

Figure 12



Cross sections of porous fiber preforms fabricated based on (a) stacking technique, (b) structured molding based on sacrificial polymer technique, and (c) structured molding technique. Cross sections of porous fibers pulled from preforms shown (d) in part (a), (e) in part (b), and (f) in part (c). (a), (b), and (d) are reproduced with permission, ©2009. Optical Society of America [140]. (c), (e), and (f) are reproduced with permission, ©2010. Optical Society of America [141].

a solvent for several days to etch away the polymer material (PMMA) residing in holes. The fibers were also left to dry for several days. The resultant fiber cross section is shown in Fig. 12(e). Although the air holes were preserved in this method, the fabrication process is very lengthy and the choice of material is limited in terms of dissolving solvent and melting temperature differences between the materials. Large melting temperature differences can result in material degradation. Moreover, the maximum porosity achieved was 29%–45%. In the second approach, the fiber preform was constructed by casting PE into a glass mold, as shown in Fig. 12(c) [141]. The glass rods were pulled out from the preform, and any residual glass is etched away before pulling into fiber. Then the resultant PE preform is drawn down using active pressurization. The pressurization is implemented not only to prevent hole closure but also to inflate the holes in order to increase the porosity (86% [141]). The resultant fiber cross section is shown in Fig. 12(f). A drawback of this approach is that active pressurization severely deforms the fiber cross section.

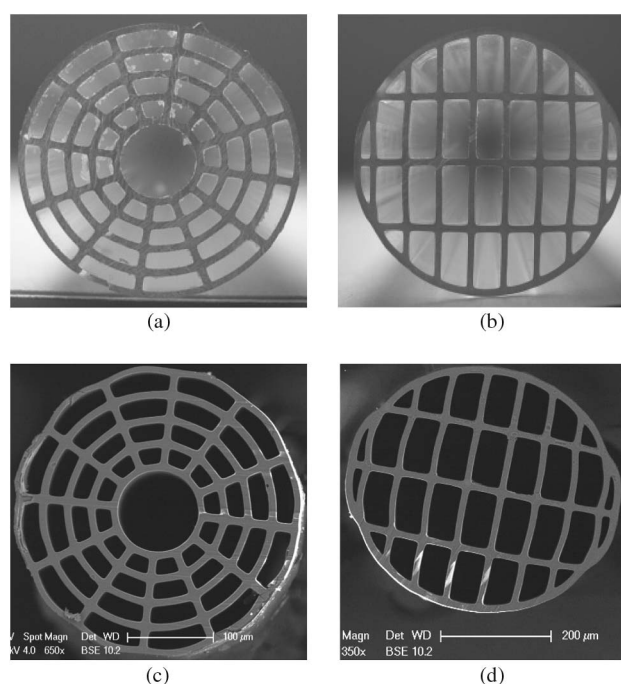
Drilling the hole pattern into a polymer preform using a computer controlled mill, and drawing the preform down to fiber, is another technique utilized for fabrication of THz solid- and hollow-core microstructured polymer waveguides [39,50]. This technique is not adequate for fabrication of highly porous fibers because the drilling process of the holes in the preform is very time consuming for a large number of holes. This method also has restricted maximum porosity due to the mechanical constraints of the hole size and the wall thickness between the holes [142]. Furthermore, the shape of the holes is limited to the circular shape.

Among all these methods, the extrusion technique is best suited for fabricating polymer porous fiber preforms [43,137]. In this approach the preforms with macroscopic-scale (mm-scale) features are manufactured using the extrusion

technique, which has been demonstrated to be viable not only for soft glasses [143] but also for polymers [144]. The preforms are extruded by heating up a bulk polymer/glass billet to a temperature at which the material becomes soft. The soft material is then forced through an extrusion die at a fixed speed. The die exit geometry determines the preform cross section. An advantage of this technique is that it is possible to fabricate preforms with non-circular air holes [143,145]. Figures 13(a) and 13(b) show the preforms of two types of porous fibers, i.e., with symmetrical and asymmetrical features, respectively, which have been fabricated by exploiting the extrusion technique [43]. The advantage of using the extrusion technique for preform fabrication is that the preform structure itself has high porosity since it is the scaled-up version of the final fiber structure; see Figs. 13(c) and 13(d). Thus no active pressurization, which deforms the fiber structure, is required during the drawing process [137]. High porosity fiber preforms, with more than 60% porosity, and non-circular air holes are not achievable with other preform fabrication techniques, e.g., casting and drilling techniques. The porosity measured from images of the preform and final fiber was 8%–10% lower than the porosity of the waveguides designed due to rounding of the corners and thickening of the struts during the fabrication process. The porosity of the spider-web and rectangular porous waveguides given by the die designs was 67% and 71%, respectively, while the porosity of the fabricated waveguides was measured to be 57% and 65%, respectively. This is small compared to the deformation of the fibers fabricated with other techniques.

Three different techniques have been used to characterize these porous waveguides. In the first approach, three different lengths of a porous fiber were

Figure 13

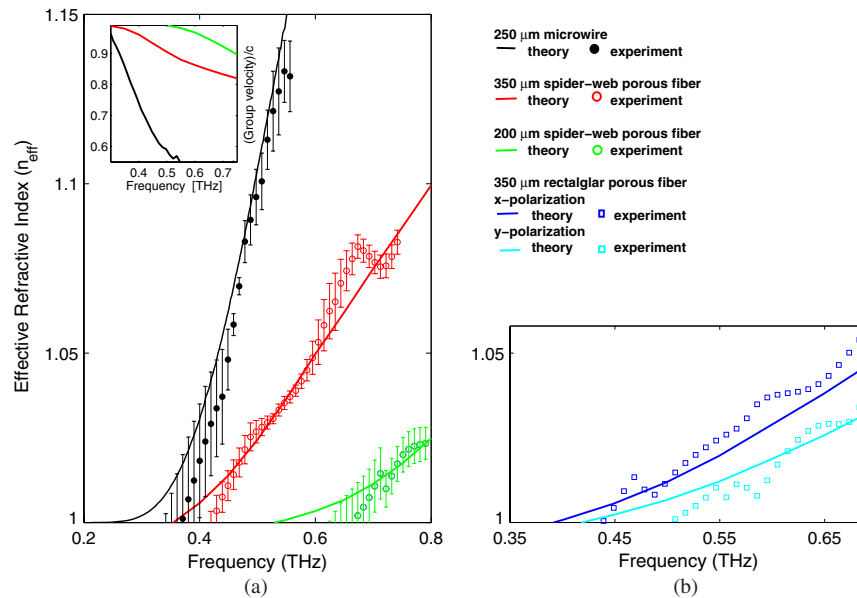


Images of SEM cross sections of (a) spider-web and (b) rectangular porous preforms fabricated based on the extrusion technique. Images of SEM cross sections of (c) spider-web and (d) rectangular porous waveguides. Reproduced with permission, ©2009. Optical Society of America [43].

directly positioned on the emitter and detector [43]. Using this technique, the dispersion characteristics of these waveguides were compared with their micro-wire counterparts [Fig. 14(a)], and the birefringence characteristics [$|N_x - N_y| \cong 0.012$ at 0.65 THz as shown in Fig. 14(b)] were for the first time, to the best of our knowledge, reported experimentally. Three main issues were identified for introducing high uncertainty in the loss measurement: the quality and repeatability of the cleaved end-face of the porous fibers, alignment of the fiber tips with the detector and emitter, and slight curvature of the fiber. In order to conduct a sufficiently precise cut-back-based loss measurement, a rapid, reproducible, and *in situ* cleaving method is required. These waveguides are easily squashed and deformed during the cleaving process when conventional blades are used for this purpose [137,146]. It is essential to have a reproducible cleaving technique in order to observe a fabricated fiber cross section without deformation during the cleaving process and to conduct loss measurement, as we observe later. This can be achieved utilizing a UV laser [137], which leads to a complicated experimental setup.

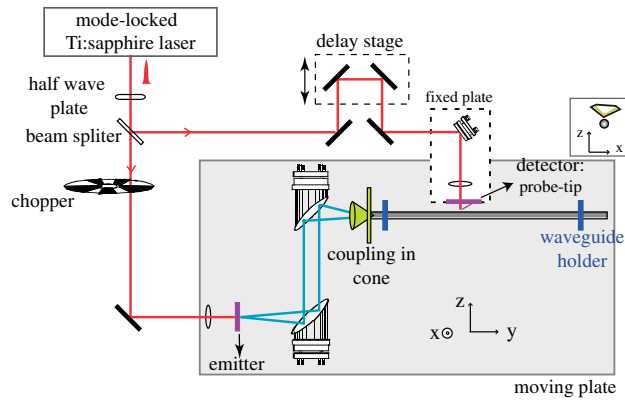
In the second approach, a directional coupler based method, in which a secondary waveguide was located and translated along the fiber being characterized, was used to characterize and eliminate cleaving issues [140]. The disadvantage of this approach is that the coupling efficiency and length of the coupler are frequency dependent, which complicates the interpretation of the results. Maintaining a constant separation between the two waveguides is challenging. Furthermore, a bolometer was employed as a detector; hence, fiber dispersion

Figure 14



Effective refractive indices of a 200 μm (green) and a 350 μm (red) diameter of spider-web porous fiber, a 250 μm diameter of microwire (black), and a 350 μm diameter of rectangular porous fiber *x*-polarization (blue) and *y*-polarization (cyan) as a function of frequency. The solid lines represent the theoretical results based on the real fiber, while the circles represent the measured experimental results. Reproduced with permission, ©2009. Optical Society of America [43].

Figure 15

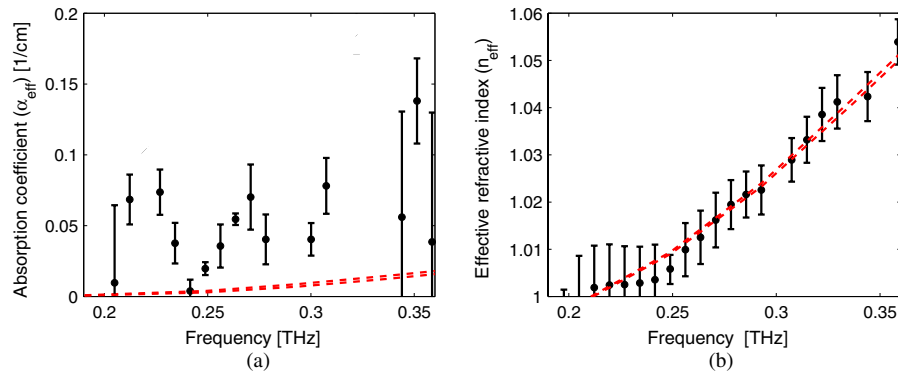


Schematic of the THz TDS setup employed for characterization of porous fibers. Two parabolic mirrors and a metallic cone are employed to couple the THz pulses into the waveguide. Reprinted with permission from S. Atakaramians, Appl. Phys. Lett. **98**, 121104 (2011) [47]. Copyright [2011] American Institute of Physics LLC.

properties were still not accessible. Average losses as low as 0.01 cm^{-1} have been reported [140] with this approach.

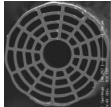
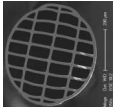

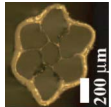
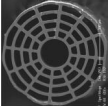
In the third approach, a micromachined photoconductive probe-tip was used to directly sample the evanescent THz electric field in the time domain in the vicinity of the fiber surface, as shown in Fig. 15 [47]. A photoconductive antenna array is used as the emitter [147]. This approach simultaneously measures both the absorption coefficient (α_{eff}) and the effective refractive index (n_{eff}) of the propagating modes of a porous fiber, shown respectively in Figs. 16(a) and 16(b). Losses less than 0.08 cm^{-1} are measured at the frequency range of 0.2 to 0.35 THz, with the minimum of 0.003 cm^{-1} at 0.24 THz. Normalized

Figure 16



(a) Absorption coefficient, α_{eff} , and (b) effective refractive index of the propagating fundamental mode in a $600 \mu\text{m}$ COC spider-web porous fiber: black dots and red dashed lines represent the measured and theoretical values, respectively. The fiber cross section is shown in the inset of (a), and the calculated normalized group velocity is shown in the inset of (b). Reprinted with permission from S. Atakaramians, Appl. Phys. Lett. **98**, 121104 (2011) [47]. Copyright [2011] American Institute of Physics LLC.

Table 5. Summary of THz Porous-Core Dielectric Waveguides^{a,b,c,d}

Waveguide	Dimensions	Material	α_{eff} [cm ⁻¹]	n_{eff}	Remarks	Refs.
	$D = 200 \text{ }\mu\text{m}$, $l = 15 \text{ mm}$, Porosity = 57%	PMMA	—	$n_{\text{eff}} < 1$, (0.35 < f < 0.8)	Extrusion technique. Uncertainty in the loss measurement due to cleaving.	[43]
	$D = 350 \text{ }\mu\text{m}$, $l = 30 \text{ mm}$, Porosity = 64%	PMMA	—	$n_{\text{eff}} < 1.05$ (0.35 < f < 0.8)	Birefringence 0.012 at 0.65 THz.	[43]
	$D = 350 \text{ }\mu\text{m}$, $l = 6 \text{ mm}$, Porosity = 40%	PE	0.001 at $f = 0.3 \text{ THz}$	—	Directional coupler technique. Detector: bolometer. Only loss reported.	[140]
	$D = 775 \text{ }\mu\text{m}$, $l = 23 \text{ cm}$, Porosity = 86%	PE	<0.05 (0.18 < f < 0.3 THz)	—	Deformation of structure during draw. Only loss reported.	[141]
	$D = 600 \text{ }\mu\text{m}$, $l = 75 \text{ mm}$, Porosity = 64%	COC	<0.08 (0.2 < f < 0.35 THz)	$n_{\text{eff}} < 1.05$ (0.2 < f < 0.35 THz)	Detector: near-field probe-tip. Both waveguide parameters reported.	[47]

^a The first and second images are reproduced with permission, ©2009, Optical Society of America [43].

^b The third image is reproduced with permission, ©2009, Optical Society of America [140].

^c The fourth image is reproduced with permission, ©2010, Optical Society of America [141].

^d The fifth image is reprinted with permission from S. Atakaramians, Appl. Phys. Lett. **98**, 121104 (2011) [47]. Copyright [2011] American Institute of Physics LLC.

group velocity greater than 0.8, which is equivalent to dispersion values between -1.3 and -0.5 ps/m/ μm for $0.2 \text{ THz} < f < 0.35 \text{ THz}$, is evaluated. This approach also allowed direct measurement of the evanescent electric-field distribution of the porous fiber. It is worth noting that porous-core waveguides with low porosity, e.g., 4% porosity [127], have similar characteristics to those of a microwire; i.e., the frequencies where the diameter of the waveguide is comparable to the wavelength of the effective material losses follow the trend of bulk material losses, while for diameters that are smaller than the operating wavelength, the effective material losses are less than those of the bulk material.

The guiding mechanism in porous-core waveguides is based on total internal reflection, the same guiding mechanism as in solid-core waveguides. These waveguides have porous transverse cross sections, i.e., subwavelength features in the core, which leads to enhancement and confinement of the field within the holes. These porous-core waveguides offer lower frequency dependent loss and dispersion compared to their solid-core counterparts, microwires. Furthermore, introducing asymmetrical discontinuity leads to high birefringence, which is comparable to the recently achieved high birefringence in PCFs. These waveguides have the potential to be employed as biosensors. A summary of all the key parameters discussed for the above porous-core waveguides is presented in Table 5. It should be noted that the porous-core honeycomb bandgap THz fiber reported theoretically by Nielsen *et al.* [67] is different from the porous-core waveguides discussed above. Although the waveguide physically has a porous core, the guiding mechanism is due to the formation of bandgaps. The refractive index of the core is lower than that of the cladding. The porous-core feature makes the manufacturing process of such waveguides more straightforward.

5. Conclusion and Final Remarks

We have reviewed different THz non-planar dielectric waveguide structures in terms of loss, dispersion, and proposed experimental arrangements. We have divided the dielectric waveguide solutions proposed in the literature into three classes: hollow-core, solid-core, and porous-core waveguides.

The material absorption is almost zero for hollow-core waveguides since the THz radiation is predominately confined in the air core. The confined mode in the core makes them good candidates for sensing applications. However, the dimension of these waveguides is in the order of a few millimeters. This dimension leads to rigid and large waveguides, which are not practical for the integrated THz devices. Another drawback of these waveguides is that their low-loss and -dispersion behavior is limited to a transmission window, which is narrow compared to the THz spectrum. A third drawback of these waveguides is the multimode operation due to the large core sizes. Although reducing the core size eliminates higher-order modes, it increases the attenuation of the fundamental mode [112].

In contrast, THz radiation propagating in the solid-core dielectric waveguides suffers from material absorption. Two solutions have been proposed to decrease the loss value of a solid-core waveguide: the first uses the waveguide structures from low-loss dielectric materials such as TOPAS. The minimum losses achieved in this way are limited to the bulk material loss. The second pushes most of the propagating mode into the air, decreasing the waveguide dimension (subwavelength air-clad waveguides). The disadvantage of such an approach is that the mode becomes loosely confined to the waveguide and susceptible to any perturbation.

Porous-core waveguides offer better confinement and lower losses due to less material residing in the core compared to solid-core waveguides. These waveguides have great potential for sensing applications. However, a large portion of the power is still in the air, making the waveguides susceptible to any perturbation.

The emergence of metamaterials has opened new opportunities in improving THz waveguides [114,115]. It has been shown that metamaterial waveguides can guide a mode even when the core diameter is more than 10 times smaller than the operating wavelength. Therefore, a reasonable direction for the future of THz waveguides is toward hollow-core waveguides with metamaterial cladding. These waveguides are expected to have low losses similar to hollow-core waveguides and to be flexible similar to solid/porous-core subwavelength waveguides.

Acknowledgments

This research was partly supported under the Australian Research Council (ARC) Discovery Projects Funding Schemes (DP120103942, DP120100200, and DP1097281) and by the ARC Centre of Excellence for Ultrahigh bandwidth Devices for Optical Systems (CUDOS, project number CE110001018). T. M. Monro acknowledges the support of an ARC Federation Fellowship.

References and Notes

1. D. Abbott and X.-C. Zhang, "Scanning the issue: T-ray imaging, sensing, and retection," *Proc. IEEE* **95**, 1509–1513 (2007).
2. W. Withayachumnankul, G. M. Png, X. Yin, S. Atakaramians, I. Jones, H. Lin, B. S.-Y. Ung, J. Balakrishnan, B. W.-H. Ng, B. Ferguson, S. P. Mickan, B. M. Fischer, and D. Abbott, "T-ray sensing and imaging," *Proc. IEEE* **95**, 1528–1558 (2007).
3. D. Mittleman, *Sensing with Terahertz Radiation* (Springer-Verlag, 2003).
4. Y.-S. Lee, *Principles of Terahertz Science and Technology* (Springer Science+Business Media, 2009).
5. S. L. Dexheimer, *Terahertz Spectroscopy Principles and Applications* (CRC Press, 2008).
6. G. Keiser, *Optical Fiber Communications*, 2nd ed. (McGraw-Hill, 1991).
7. J. M. López-Higuera, L. R. Cobo, A. Q. Incera, and A. Cobo, "Fiber optic sensors in structural health monitoring," *J. Lightwave Technol.* **29**, 587–608 (2011).
8. D. R. Walt, "Fibre optic microarrays," *Chem. Soc. Rev.* **39**, 38–50 (2010).

9. J. Faist, F. Capasso, D. L. Sivco, C. Sirtori, A. L. Hutchinson, and A. Y. Cho, "Quantum cascade laser," *Science* **264**, 553–556 (1994).
10. V. R. Almeida, Q. Xu, C. A. Barrios, and M. Lipson, "Guiding and confining light in void nanostructure," *Opt. Lett.* **29**, 1209–1211 (2004).
11. T. M. Monro, "Beyond the diffraction limit," *Nat. Photonics* **1**, 89–90 (2007).
12. K. Eshraghian, "SoC emerging technologies," *Proc. IEEE* **94**, 1197–1213 (2006).
13. J. S. Melinger, S. S. Harsha, N. Laman, and D. Grischkowsky, "Guided-wave terahertz spectroscopy of molecular solids [Invited]," *J. Opt. Soc. Am. B* **26**, A79–A89 (2009).
14. M. Nagel, M. Först, and H. Kurz, "THz biosensing devices: fundamentals and technology," *J. Phys. Condens. Matter* **18**, S601–S618 (2006).
15. S. A. Maier, S. R. Andrews, L. Martin-Moreno, and F. J. Garcia-Vidal, "Terahertz surface plasmon-polariton propagation and focusing on periodically corrugated metal wires," *Appl. Phys. Lett.* **97**, 176805 (2006).
16. V. Astley, K. S. Reichel, J. Jones, R. Mendis, and D. M. Mittleman, "Terahertz multichannel microfluidic sensor based on a parallel-plate waveguide resonant cavities," *Appl. Phys. Lett.* **100**, 231108 (2012).
17. G. Gallot, S. P. Jamison, R. W. McGowan, and D. Grischkowsky, "Terahertz waveguides," *J. Opt. Soc. Am. B* **17**, 851–863 (2000).
18. R. Mendis and D. Grischkowsky, "Undistorted guided-wave propagation of subpicosecond terahertz pulses," *Opt. Lett.* **26**, 846–848 (2001).
19. S. Atakaramians, "Terahertz waveguides: a study of microwires and porous fibres," Ph.D. thesis (The University of Adelaide, 2011).
20. D. H. Auston, A. M. Johnson, P. R. Smith, and J. C. Bean, "Picosecond optoelectronic detection, sampling, and correlation-measurements in amorphous-semiconductors," *Appl. Phys. Lett.* **37**, 371–373 (1980).
21. P. R. Smith, D. H. Auston, and W. M. Augustyniak, "Measurement of GaAs field-effect transistor electronic impulse-response by picosecond optical electronics," *Appl. Phys. Lett.* **39**, 739–741 (1981).
22. M. B. Ketchen, D. Grischkowsky, T. C. Chen, C. C. Chi, N. I. Duling, N. J. Halas, J.-M. Halbout, J. A. Kash, and G. P. Li, "Generation of subpicosecond electrical pulses on coplanar transmission lines," *Appl. Phys. Lett.* **48**, 751–753 (1986).
23. D. Grischkowsky, "Optoelectronic characterization of transmission lines and waveguides by terahertz time-domain spectroscopy," *IEEE J. Sel. Top. Quantum Electron.* **6**, 1122–1135 (2000).
24. D. Grischkowsky, N. I. Duling, J. C. Chen, and C.-C. Chi, "Electromagnetic shock waves from transmission lines," *Phys. Rev. Lett.* **59**, 1663–1666 (1987).
25. K. C. Gupta, R. Grag, I. Bahl, and P. Bhartia, *Microstrip Lines and Slotlines*, 2nd ed. (Artech House, 1996).
26. C. P. Wen, "Coplanar waveguide: a surface strip transmission line suitable for nonreciprocal gyromagnetic device applications," *IEEE Trans. Microwave Theory Tech.* **MT-17**, 1087–1090 (1969).
27. C. Nguyen, *Analysis Methods for RF, Microwave, and Millimeter-Wave Planar Transmission Line Structures* (Wiley, 2001).
28. D. E. Cooper, "Picosecond optoelectronic measurement of microstrip dispersion," *Appl. Phys. Lett.* **47**, 33–35 (1985).
29. R. Sprik, I. N. Duling, C. C. Chi, and D. Grischkowsky, "Far infrared-spectroscopy with subpicosecond electrical pulses on transmission-lines," *Appl. Phys. Lett.* **51**, 548–550 (1987).

30. W. Withayachumnankul, "Engineering aspects of terahertz time-domain spectroscopy," Ph.D. thesis (The University of Adelaide, 2009).
31. R. W. McGowan, G. Gallot, and D. Grischkowsky, "Propagation of ultra-wideband short pulses of terahertz radiation through submillimeter-diameter circular waveguides," *Opt. Lett.* **24**, 1431–1433 (1999).
32. M. van Exter, C. Fattinger, and D. Grischkowsky, "High-brightness terahertz beams characterized with an ultrafast detector," *Appl. Phys. Lett.* **55**, 337–339 (1989).
33. M. van Exter, C. Fattinger, and D. Grischkowsky, "Terahertz time-domain spectroscopy of water vapor," *Opt. Lett.* **14**, 1128–1130 (1989).
34. A. Treizebre, T. Akalin, and B. Bocquet, "Planar excitation of Goubau transmission lines for THz bioMEMS," *IEEE Microw. Wirel. Compon. Lett.* **15**, 886–888 (2005).
35. T. Akalin, A. Treizebre, and B. Bocquet, "Single-wire transmission lines at terahertz frequencies," *IEEE Trans. Microwave Theory Tech.* **54**, 2762–2767 (2006).
36. Y. Xu and R. G. Bosisio, "A comprehensive study on the planar type of Goubau line for millimetre and submillimetre wave integrated circuits," *IET Microw. Antennas Propag.* **1**, 681–687 (2007).
37. L. Dazhang, J. Cunningham, M. B. Byrne, S. Khanna, C. D. Wood, A. D. Burnett, S. M. Ershad, E. H. Linfield, and A. G. Davies, "On-chip terahertz Goubau-line waveguides with integrated photoconductive emitters and mode-discriminating detectors," *Appl. Phys. Lett.* **95**, 092903 (2009).
38. L.-J. Chen, H.-W. Chen, T.-F. Kao, J.-Y. Lu, and C.-K. Sun, "Low-loss subwavelength plastic fiber for terahertz waveguiding," *Opt. Lett.* **31**, 308–310 (2006).
39. C. S. Ponseca, R. Pobre, E. Estacio, N. Sarukura, A. Argyros, M. C. J. Large, and M. A. van Eijkelenborg, "Transmission of terahertz radiation using a microstructured polymer optical fiber," *Opt. Lett.* **33**, 902–904 (2008).
40. C.-H. Lai, Y.-C. Hsueh, H.-W. Chen, Y.-J. Huang, H.-C. Chang, and C.-K. Sun, "Low-index terahertz pipe waveguides," *Opt. Lett.* **34**, 3457–3459 (2009).
41. T.-I. Jeon, J. Zhang, and K. W. Goossen, "THz Sommerfeld wave propagation on a single metal wire," *Appl. Phys. Lett.* **86**, 161904 (2005).
42. M. Wächter, M. Nagel, and H. Kurz, "Frequency-dependent characterization of THz Sommerfeld wave propagation on single-wires," *Opt. Express* **13**, 10815–10822 (2005).
43. S. Atakaramians, S. Afshar Vahid, M. Nagel, H. Ebendorff-Heidepriem, B. M. Fischer, D. Abbott, and T. M. Monro, "THz porous fibers: design, fabrication and experimental characterization," *Opt. Express* **17**, 14053–14062 (2009).
44. Y. Kawano and K. Ishibashi, "An on-chip near-field terahertz probe and detector," *Nat. Photonics* **2**, 618–621 (2008).
45. M. Wächter, M. Nagel, and H. Kurz, "Tapered photoconductive terahertz field probe tip with subwavelength spatial resolution," *Appl. Phys. Lett.* **95**, 041112 (2009).
46. M. Wächter, M. Nagel, and H. Kurz, "Metallic slit waveguide for dispersion-free low-loss terahertz signal transmission," *Appl. Phys. Lett.* **90**, 061111 (2007).

47. S. Atakaramians, S. Afshar V., H. Rasmussen, O. Bang, T. M. Monro, and D. Abbott, "Direct probing of evanescent field for characterization of porous terahertz fibers," *Appl. Phys. Lett.* **98**, 121104 (2011).
48. K. Wang and D. M. Mittleman, "Metal wires for terahertz wave guiding," *Nature* **432**, 376–379 (2004).
49. B. Bowden, J. A. Harrington, and O. Mitrofanov, "Silver/polystyrene-coated hollow glass waveguides for the transmission of terahertz radiation," *Opt. Lett.* **32**, 2945–2947 (2007).
50. K. Nielsen, H. K. Rasmussen, A. J. L. Adam, P. C. M. Planken, O. Bang, and P. U. Jepsen, "Bendable, low-loss Topas fibers for the terahertz frequency range," *Opt. Express* **17**, 8592–8601 (2009).
51. R. Mendis, "First broadband experimental study of planar THz waveguides," Ph.D. thesis (Oklahoma State University, 2001).
52. J. Werner, E. Kapon, A. C. V. Lehmen, R. Bhat, E. Colas, N. G. Stoffel, and S. A. Schwarz, "Reduced optical waveguide losses of a partially disordered GaAs/AlGaAs single quantum well laser structure for photonic integrated circuits," *Appl. Phys. Lett.* **53**, 1693–1695 (1988).
53. M. Nagel, A. Marchewka, and H. Kurz, "Low-index discontinuity terahertz waveguides," *Opt. Express* **14**, 9944–9954 (2006).
54. R. Mendis and D. Grischkowsky, "THz interconnect with low-loss and low-group velocity dispersion," *IEEE Microw. Wirel. Compon. Lett.* **11**, 444–446 (2001).
55. R. Mendis and D. M. Mittleman, "Comparison of the lowest-order transverse-electric (TE_1) and transverse-magnetic (TEM) modes of the parallel-plate waveguide for terahertz pulse applications," *Opt. Express* **17**, 14839–14850 (2009).
56. R. Mendis and D. M. Mittleman, "An investigation of the lowest-order transverse-electric (TE_1) mode of the parallel-plate waveguide for THz pulse propagation," *J. Opt. Soc. Am. B* **26**, A6–A13 (2009).
57. T.-I. Jeon and D. Grischkowsky, "Direct optoelectronic generation and detection of sub-ps-electrical pulses on sub-mm-coaxial transmission lines," *Appl. Phys. Lett.* **85**, 6092–6094 (2004).
58. A. Bingham and D. Grischkowsky, "Terahertz 2-D photonic crystal waveguides," *IEEE Microw. Wireless Compon. Lett.* **18**, 428–430 (2008).
59. T.-I. Jeon and D. Grischkowsky, "THz Zenneck surface wave (THz surface plasmon) propagation on a metal sheet," *Appl. Phys. Lett.* **88**, 061113 (2006).
60. M. J. King and J. C. Wiltse, "Surface-wave propagation on coated or uncoated metal wires at millimeter wavelengths," *IRE Trans. Antennas Propag.* **10**, 246–254 (1962).
61. J. Dai, J. Zhang, W. Zhang, and D. Grischkowsky, "THz time-domain spectroscopy characterization of the far-infrared absorption and index of refraction of high resistivity, float-zone silicon," *J. Opt. Soc. Am. B* **21**, 1379–1386 (2004).
62. B. M. Fischer, "Broadband THz time-domain spectroscopy of biomolecules," Ph.D. thesis (University of Freiburg, 2005).
63. Y.-S. Jin, G.-J. Kim, and S.-G. Jeon, "Terahertz dielectric properties of polymers," *J. Korean Phys. Soc.* **49**, 513–517 (2006).
64. J. Balakrishnan, B. M. Fischer, and D. Abbott, "Sensing the hygroscopicity of polymer and copolymer materials using terahertz time-domain spectroscopy," *Appl. Opt.* **48**, 2262–2266 (2009).

65. P. D. Cunningham, N. N. Valdes, F. A. Vallejo, L. M. Hayden, B. Polishak, X.-H. Zhou, J. Luo, A. K.-Y. Jen, J. C. Williams, and R. J. Twieg, "Broad-band terahertz characterization of the refractive index and absorption of some important polymeric and organic electro-optic materials," *J. Appl. Phys.* **109**, 043505 (2011).
66. F. Brechet, P. Roy, J. Marcou, and D. Pagnoux, "Single-mode propagation into depressed-core-index photonic-bandgap fibre designed for zero-dispersion propagation at short wavelengths," *Electron. Lett.* **36**, 514–515 (2000).
67. K. Nielsen, H. K. Rasmussen, P. U. Jepsen, and O. Bang, "Porous-core honeycomb bandgap THz fiber," *Opt. Lett.* **36**, 666–668 (2011).
68. T. M. Monro and H. Ebendorff-Heidepriem, "Progress in microstructured optical fibers," *Annu. Rev. Mater. Sci.* **36**, 467–495 (2006).
69. J.-Y. Lu, C.-P. Yu, H.-C. Chang, H.-W. Chen, Y.-T. Li, C.-L. Pan, and C.-K. Sun, "Terahertz air-core microstructure fiber," *Appl. Phys. Lett.* **92**, 064105 (2008).
70. H. Han, H. Park, M. Cho, and J. Kim, "Terahertz pulse propagation in a plastic photonic crystal fiber," *Appl. Phys. Lett.* **80**, 2634–2636 (2002).
71. M. Cho, J. Kim, H. Park, Y. Han, K. Moon, E. Jung, and H. Han, "Highly birefringent terahertz polarization maintaining plastic photonic crystal fibers," *Opt. Express* **16**, 7–12 (2008).
72. J. A. Harrington, *Infrared Fibers and Their Applications* (SPIE, 2004).
73. F. Benabid, P. J. Roberts, F. Couny, and P. S. Light, "Light and gas confinement in hollow-core photonic crystal fibre based photonic microcells," *J. Eur. Opt. Soc. Rapid Pub.* **4**, 09004 (2009).
74. K. J. Rowland, "Guiding light in low-index media via multilayer waveguides," Ph.D. thesis (The University of Adelaide, 2010).
75. J. C. Knight, T. A. Birks, P. S. Russell, and D. M. Atkin, "All-silica single-mode optical fiber with photonic crystal cladding," *Opt. Lett.* **21**, 1547–1549 (1996).
76. J. C. Knight, J. Broeng, T. A. Birks, and P. S. J. Russell, "Photonic band gap guidance in optical fibers," *Science* **282**, 1476–1478 (1998).
77. B. Temelkuran, S. D. Hart, G. Benoit, J. D. Joannopoulos, and Y. Fink, "Wavelength-scalable hollow optical fibres with large photonic bandgaps for CO₂ laser transmission," *Nature* **420**, 650–653 (2002).
78. T. Katagiri, Y. Matsuura, and M. Miyagi, "Photonic bandgap fiber with a silica core and multilayer dielectric cladding," *Opt. Lett.* **29**, 557–559 (2004).
79. F. Couny, F. Benabid, and P. S. Light, "Large-pitch Kagome-structured hollow-core photonic crystal fiber," *Opt. Lett.* **31**, 3574–3576 (2006).
80. A. Argyros and J. Pla, "Hollow-core polymer fibers with a Kagome lattice: potential for transmission in the infrared," *Opt. Express* **15**, 7713–7719 (2007).
81. F. Couny, P. J. Roberts, T. A. Birks, and F. Benabid, "Square-lattice large-pitch hollow-core photonic crystal fiber," *Opt. Express* **16**, 20626–20636 (2008).
82. A. Argyros, S. G. Leon-Saval, J. Pla, and A. Docherty, "Antiresonant reflection and inhibited coupling in hollow-core square lattice optical fibers," *Opt. Express* **16**, 5642–5648 (2008).
83. K. J. Rowland, S. Afshar V., and T. M. Monro, "Bandgaps and antiresonances in integrated-ARROWs and Bragg fibers; a simple model," *Opt. Express* **16**, 17935–17951 (2008).

84. K. J. Rowland, S. Afshar V., A. Stolyarov, Y. Fink, and T. M. Monro, "Bragg waveguides with low-index liquid cores," *Opt. Express* **20**, 48–62 (2012).
85. T. Hidaka, H. Minamide, H. Ito, S.-I. Maeta, and T. Akiyama, "Ferroelectric PVDF cladding THz waveguide," *Proc. SPIE* **5135**, 70–77 (2003).
86. T. Hidaka, I. Morohashi, K. Komori, H. Nakagawa, and H. Ito, "THz wave hollow waveguide with ferroelectric PVDF polymer as the cladding material," in *IEEE Conference on Lasers and Electro-Optics Europe* (IEEE, 2000), paper CWF7.
87. T. Hidaka, H. Minamide, H. Ito, J.-I. Nishizawa, K. Tamura, and S. Ichikawa, "Ferroelectric PVDF cladding terahertz waveguide," *J. Lightwave Technol.* **23**, 2469–2473 (2005).
88. M. Yan and N. A. Mortensen, "Hollow-core infrared fiber incorporating metal-wire metamaterial," *Opt. Express* **17**, 14851–14864 (2009).
89. J. A. Harrington, R. George, P. Pedersen, and E. Mueller, "Hollow polycarbonate waveguides with inner cu coatings for delivery of terahertz radiation," *Opt. Express* **12**, 5263–5268 (2004).
90. T. Ito, Y. Matsuura, M. Miyagi, H. Minamide, and H. Ito, "Flexible terahertz fiber optics with low bend-induced losses," *J. Opt. Soc. Am. B* **24**, 1230–1235 (2007).
91. O. Mitrofanov, R. James, F. A. Fernandez, T. K. Mavrogordatos, and J. A. Harrington, "Reducing transmission losses in hollow THz waveguides," *IEEE Trans. Terahertz Sci. Technol.* **1**, 124–132 (2011).
92. Y. Matsuura and E. Takeda, "Hollow optical fibers loaded with an inner dielectric film for terahertz broadband spectroscopy," *J. Opt. Soc. Am. B* **25**, 1949–1954 (2008).
93. X. L. Tang, Y. W. Shi, Y. Matsuura, K. Iwai, and M. Miyagi, "Transmission characteristics of terahertz hollow fiber with an absorptive dielectric inner-coating film," *Opt. Lett.* **34**, 2231–2233 (2009).
94. D. R. Chen and H. B. Chen, "A novel low-loss terahertz waveguide: polymer tube," *Opt. Express* **18**, 3762–3767 (2010).
95. F. Gérôme, R. Jamier, J. L. Auguste, G. Humbert, and J. M. Blondy, "Simplified hollow-core photonic crystal fiber," *Opt. Lett.* **35**, 1157–1159 (2010).
96. R. A. Correa and J. Knight, "Specialty fibers: novel process eases production of hollow-core fiber," *Laser Focus World* **44**, 67–71 (2008).
97. The confinement loss for axial mode propagation is the loss of power through the transverse structure, which is also known as leakage loss.
98. Y. F. Geng, X. L. Tan, P. Wang, and J. Q. Yao, "Transmission loss and dispersion in plastic terahertz photonic band-gap fibers," *Appl. Phys. B* **91**, 333–336 (2008).
99. P. J. Roberts, F. Couny, H. Sabert, B. J. Mangan, T. A. Birks, J. C. Knight, and P. S. J. Russell, "Loss in solid-core photonic crystal fibers due to interface roughness scattering," *Opt. Express* **13**, 7779–7793 (2005).
100. Y. F. Geng, X. L. Tan, K. Zhong, P. Wang, and J. Q. Yao, "Low loss plastic terahertz photonic band-gap fibers," *Chin. Phys. Lett.* **25**, 3961–3963 (2008).
101. G. Ren, Y. Gong, P. Shum, X. Yu, J. Hu, G. Wang, M. O. L. Chuen, and V. Paulose, "Low-loss air-core polarization maintaining terahertz fiber," *Opt. Express* **16**, 13593–13598 (2008).

102. L. Vincetti, "Hollow core photonic band gap fiber for THz applications," *Microw. Opt. Technol. Lett.* **51**, 1711–1714 (2009).
103. L. Vincetti and A. Polemi, "Hollow core fiber for THz applications," in *Proceedings of IEEE Antennas and Propagation Society International Symposium* (IEEE, 2009), pp. 1–4.
104. M. Skorobogatiy and A. Dupuis, "Ferroelectric all-polymer hollow Bragg fibers for terahertz guidance," *Appl. Phys. Lett.* **90**, 113514 (2007).
105. R. J. Yu, B. Zhang, Y. Q. Zhang, C. Q. Wu, Z. G. Tian, and X. Z. Bai, "Proposal for ultralow loss hollow-core plastic Bragg fiber with cobweb-structured cladding for terahertz waveguiding," *IEEE Photon. Technol. Lett.* **19**, 910–912 (2007).
106. A. Dupuis, K. Stoeffler, B. Ung, C. Dubois, and M. Skorobogatiy, "Transmission measurements of hollow-core THz Bragg fibers," *J. Opt. Soc. Am. B* **28**, 896–907 (2011).
107. F. Couny, F. Benabid, P. J. Roberts, P. S. Light, and M. G. Raymer, "Generation and photonic guidance of multi-octave optical-frequency combs," *Science* **318**, 1118–1121 (2007).
108. L. Vincetti, "Numerical analysis of plastic hollow core microstructured fiber for terahertz applications," *Opt. Fiber Technol.* **15**, 398–401 (2009).
109. Y. Y. Wang, N. V. Wheeler, F. Couny, P. J. Roberts, and F. Benabid, "Low loss broadband transmission in hypocycloid-core Kagome hollow-core photonic crystal fiber," *Opt. Lett.* **36**, 669–671 (2011).
110. J. Anthony, R. Leonhardt, S. G. Leon-Saval, and A. Argyros, "THz propagation in Kagome hollow-core microstructured fibers," *Opt. Express* **19**, 18470–18478 (2011).
111. D. S. Wu, A. Argyros, and S. G. Leon-Saval, "Reducing the size of hollow terahertz waveguides," *J. Lightwave Technol.* **29**, 97–103 (2011).
112. L. Vincetti, "Single-mode propagation in triangular tube lattice hollow-core terahertz fibers," *Opt. Commun.* **283**, 979–984 (2010).
113. W. Withayachumnankul and D. Abbott, "Metamaterial in the terahertz regime," *IEEE Photon. J.* **1**, 99–118 (2009).
114. A. Ishikawa, S. Zhang, D. A. Genov, G. Bartal, and X. Zhang, "Deep sub-wavelength THz waveguides using gap magnetic plasmon," *Phys. Rev. Lett.* **102**, 043904 (2009).
115. S. Atakaramians, A. Argyros, S. C. Fleming, and B. T. Kuhlmeier, "Hollow-core waveguides with uniaxial metamaterial cladding: modal equations and guidance conditions," *J. Opt. Soc. Am. B* **29**, 2462–2477 (2012).
116. S. Atakaramians, A. Argyros, S. C. Fleming, and B. T. Kuhlmeier, "Hollow-core uniaxial metamaterial clad fibers with dispersive metamaterials," *J. Opt. Soc. Am. B* **30**, 851–867 (2013).
117. S. P. Jamison, R. W. McGowan, and D. Grischkowsky, "Single-mode waveguide propagation and reshaping of sub-ps terahertz pulses in sapphire fibers," *Appl. Phys. Lett.* **76**, 1987–1989 (2000).
118. R. Mendis and D. Grischkowsky, "Plastic ribbon THz waveguides," *J. Appl. Phys.* **88**, 4449–4451 (2000).
119. B. Bowden, J. A. Harrington, and O. Mitrofanov, "Low-loss modes in hollow metallic terahertz waveguides with dielectric coatings," *Appl. Phys. Lett.* **93**, 181104 (2008).
120. L. Tong, R. R. Gattass, J. B. Ashcom, S. He, J. Lou, M. Shen, I. Maxwell, and E. Mazur, "Subwavelength-diameter silica wires for low-loss optical wave guiding," *Nature* **426**, 816–819 (2003).

121. S. Atakaramians, S. Afshar Vahid, B. M. Fischer, H. Ebendorff-Heidepriem, T. M. Monro, and D. Abbott, "Low loss terahertz transmission," *Proc. SPIE* **6414**, 64140I (2006).
122. S. Afshar Vahid, S. Atakaramians, B. M. Fischer, H. Ebendorff-Heidepriem, T. M. Monro, and D. Abbott, "Low loss, low dispersion T-ray transmission in microwires," in *Proceedings of Quantum Electronics and Laser Science Conference* (IEEE, 2007), paper JWA105.
123. B. You, T. A. Liu, J. L. Peng, C. L. Pan, and J. Y. Lu, "A terahertz plastic wire based evanescent field sensor for high sensitivity liquid detection," *Opt. Express* **17**, 20675–20683 (2009).
124. B. W. You, J. Y. Lu, T. A. Liu, J. L. Peng, and C. L. Pan, "Subwavelength plastic wire terahertz time-domain spectroscopy," *Appl. Phys. Lett.* **96**, 051105 (2010).
125. H. W. Chen, C. M. Chiu, C. H. Lai, J. L. Kuo, P. J. Chiang, Y. J. Hwang, H. C. Chang, and C. K. Sun, "Subwavelength dielectric-fiber-based THz coupler," *J. Lightwave Technol.* **27**, 1489–1495 (2009).
126. J.-Y. Lu, C.-C. Kuo, C.-M. Chiu, H.-W. Chen, Y.-J. Hwang, C.-L. Pan, and C.-K. Sun, "THz interferometric imaging using subwavelength plastic fiber based THz endoscopes," *Opt. Express* **16**, 2494–2501 (2008).
127. M. Roze, B. Ung, A. Mazhorova, M. Walther, and M. Skorobogatiy, "Suspended core subwavelength fibers: towards practical designs for low-loss terahertz guidance," *Opt. Express* **19**, 9127–9138 (2011).
128. M. Goto, A. Quema, H. Takahashi, S. Ono, and N. Sarukura, "Teflon photonic crystal fiber as terahertz waveguide," *Jpn. J. Appl. Phys.* **43**, L317–L319 (2004).
129. J. R. Birch, J. D. Dromey, and J. Lesurf, "The optical-constants of some common low-loss polymers between 4 and 40 cm^{-1} ," *Infrared Phys.* **21**, 225–228 (1981).
130. J. Anthony, R. Leonhardt, A. Argyros, and M. C. J. Large, "Characterization of a microstructured Zeonex terahertz fiber," *J. Opt. Soc. Am. B* **28**, 1013–1018 (2011).
131. G. S. Wiederhecher, C. M. B. Cordeiro, F. Couny, F. Benabid, S. A. Maier, J. C. Knight, C. H. B. Crus, and H. L. Fragnito, "Field enhancement within an optical fibre with a subwavelength air core," *Nat. Photonics* **1**, 115–118 (2007).
132. A. Hassani, A. Dupuis, and M. Skorobogatiy, "Low loss porous terahertz fibers containing multiple subwavelength holes," *Appl. Phys. Lett.* **92**, 071101 (2008).
133. A. Hassani, A. Dupuis, and M. Skorobogatiy, "Porous polymer fibers for low-loss terahertz guiding," *Opt. Express* **16**, 6340–6351 (2008).
134. S. Atakaramians, S. Afshar Vahid, B. M. Fischer, D. Abbott, and T. M. Monro, "Porous fibers: a novel approach to low loss THz waveguides," *Opt. Express* **16**, 8845–8854 (2008).
135. S. Atakaramians, S. Afshar V., B. M. Fischer, D. Abbott, and T. M. Monro, "Low loss, low dispersion and highly birefringent terahertz porous fibers," *Opt. Commun.* **282**, 36–38 (2009).
136. S. Atakaramians, S. Afshar Vahid, M. Nagel, H. Ebendorff-Heidepriem, B. M. Fischer, D. Abbott, and T. M. Monro, "Experimental investigation of dispersion properties of THz porous fibers," in *33rd International IEEE Conference on Infrared, Millimeter, and Terahertz Waves* (IEEE, 2009), pp. 1–2.

137. S. Atakaramians, K. Cook, H. Ebendorff-Heidepriem, S. Afshar V., J. Canning, D. Abbott, and T. M. Monro, "Cleaving of extremely porous polymer fibers," *IEEE Photon. J.* **1**, 286–292 (2009).
138. S.-Y. Wang, "Microstructured optical fiber with improved transmission efficiency and durability," U.S. patent 6,418,258 (July 9, 2002).
139. X. Chen, M.-J. Li, N. Venkataraman, M. T. Gallagher, W. A. Wood, A. M. Crowley, J. P. Carberry, L. A. Zenteno, and K. W. Koch, "Highly birefringent hollow-core photonic bandgap fiber," *Opt. Express* **12**, 3888–3893 (2004).
140. A. Dupuis, J.-F. Allard, D. Morris, K. Stoeffler, C. Dubois, and M. Skorobogatiy, "Fabrication and THz loss measurements of porous subwavelength fibers using a directional coupler method," *Opt. Express* **17**, 8012–8028 (2009).
141. A. Dupuis, A. Mazhorova, F. Desevedavy, M. Roze, and M. Skorobogatiy, "Spectral characterization of porous dielectric subwavelength THz fibers fabricated using a microstructured molding technique," *Opt. Express* **18**, 13813–13828 (2010).
142. G. Barton, M. A. van Eijkelenborg, G. Henry, M. C. J. Large, and J. Zagari, "Fabrication of microstructured polymer optical fibers," *Opt. Fiber Technol.* **10**, 325–335 (2004).
143. H. Ebendorff-Heidepriem and T. M. Monro, "Extrusion of complex preforms for microstructured optical fibers," *Opt. Express* **15**, 15086–15096 (2007).
144. H. Ebendorff-Heidepriem, T. M. Monro, M. A. van Eijkelenborg, and M. C. J. Large, "Extruded high-na microstructured polymer optical fiber," *Opt. Commun.* **273**, 133–137 (2007).
145. H. Ebendorff-Heidepriem, R. C. Moore, and T. M. Monro, "Progress in the fabrication of the next-generation soft glass microstructured optical fibers," in *1st Workshop on Speciality Optical Fibers and Their Applications*, Vol. **1055** of AIP Conference Proceedings (AIP, 2008), pp. 95–98.
146. S. H. Law, M. A. van Eijkelenborg, G. W. Barton, C. Yan, R. Lwin, and J. Gan, "Cleaved end-face quality of microstructured polymer optical fibers," *Opt. Commun.* **265**, 513–520 (2006).
147. D. Saeedkia, R. R. Mansour, and S. Safavi-Naeini, "Analysis and design of a continuous-wave terahertz photoconductive photomixer array source," *IEEE Trans. Antennas Propag.* **53**, 4044–4050 (2005).



Shaghik Atakaramians received her bachelor's degree from Iran University of Science and Technology (IUST) and her master's degree from the University of Tehran. She was awarded first prize for the best telecommunication graduate of the Department of Electrical Engineering, IUST. In 2006, Shaghik Atakaramians joined the T-ray group of The University of Adelaide as a visiting scholar. In 2007, she was granted an Australian Endeavour International Postgraduate Research Scholarship (EIPRS) and University of Adelaide Scholarship for Postgraduate Research. She has received a number of awards including an ARC Nanotechnology Network (ARCNN) Overseas Travel Fellowship, 2008; the IEEE South Australia Travel Assistance Award, 2008; Research Abroad Scholarship, University of Adelaide, 2008; and the Incubic/Milton Chang Travel Award for CLEO/QELS conference (USA), 2007.

In 2011, she received her Ph.D. in electrical and electronic engineering with a University of Adelaide Doctoral Research Medal for outstanding research at the Ph.D. level, the Gertrude Rohan Memorial Prize for the best Ph.D. thesis in the area of information and communications technology from the School of Electrical and Electronic Engineering, and the Dean's Merit Award for an outstanding Ph.D. thesis.

In 2011, Shaghik has joined the Institute of Photonics and Optical Science (IPOS) and the ARC Centre of Excellence for Ultrahigh bandwidth Devices for Optical Systems (CUDOS) at the University of Sydney as a postdoctoral fellow. Her main interests lie in the fields of terahertz waveguides, metamaterials, guided modes, and subwavelength guidance in hyperbolic media. Shaghik is a member of the IEEE (Institute of Electrical and Electronics Engineers), OSA (Optical Society of America), and AOS (The Australian Optical Society).



Shahraam Afshar V. received his Ph.D. in physics, laser and nonlinear optics from the University of Adelaide in 2001. From 1998 to 2001 he held a lecturer position at The University of Adelaide. In 2001 he joined the fiber-optics group at The University of Ottawa as a postdoc, where he worked on fiber-optic strain and temperature sensors based on Brillouin scattering. In 2003, he received the NCIT fellowship from the National Capital Institute of Telecommunication, Canada, to work on Brillouin scattering in photonic crystal fibers. In 2005, he joined the Centre of Expertise in Photonics (CoEP) at the University of Adelaide, which was later formed into the Institute for Photonics and Advanced Sensing (IPAS). His current research within IPAS covers nonlinear optical phenomena in microstructured fibers, terahertz fibers, bandgap fibers, and chemical-biological sensing using optical fibers.



Tanya M. Monro is an ARC Federation Fellow and Director of the Institute for Photonics and Advanced Sensing (IPAS) at the University of Adelaide. IPAS pursues a transdisciplinary research agenda, bringing together physics, chemistry, and biology to create knowledge and disruptive new technologies and solve problems in health, defense, the environment, and food and wine.

Tanya is a Fellow of the Australian Academy of Science (AAS), the Australian Academy of Technological Sciences and Engineering (ATSE), and the Australian Institute of Physics (AIP). She is a member of the AAS National Committee for Physics, a member of the SA Premier's Science and Industry Council (PSIC), and an inaugural Bragg Fellow of the Royal Institution of Australia. Tanya was awarded the Australian Academy of Sciences Pawsey Medal for 2012. Tanya was South Australia's "Australian of the Year" for 2011, and in September 2011 she won the Scopus Young Researcher of the Year in Physical Science award. In 2010, she was named South Australian Scientist of the Year and was named Telstra Business Women of the Year at both national and state levels (in the Community and Government category). In 2009, Tanya was named the Emerging Leader in the Science category in

The Weekend Australian Magazine's Emerging Leader awards. In 2008 she won the Prime Minister's Malcolm McIntosh Prize for Physical Scientist of the Year, and in 2007–2008, she was the “Women in Physics Lecturer” for the Australian Institute of Physics. In 2006, *Cosmos Magazine* presented Tanya with a Bright Spark Award.

Tanya obtained her Ph.D. in physics in 1998 from The University of Sydney, for which she was awarded the Bragg Gold Medal for the best physics Ph.D. in Australia in that year. In 2000, she received a Royal Society University Research Fellowship at the Optoelectronics Research Centre at the University of Southampton in the UK. She came to the University of Adelaide in 2005 as inaugural Chair of Photonics. She has published more than 500 papers in refereed journals and conference proceedings and has raised more than \$86M for research. As well as being active in research and research leadership, she serves on international, national, and state committees and boards on matters of science and research policy and science evaluation and assessment.



Derek Abbott received a BSc (Hons) in physics from Loughborough University of Technology, UK. He obtained his Ph.D. in electrical and electronic engineering from The University of Adelaide, Australia, under Kamran Eshraghian and Bruce R. Davis. From 1978 to 1986, he worked at the GEC Hirst Research Centre, London, UK, in the area of semiconductors and optoelectronics. Upon migration to Australia, he worked for Austek Microsystems, South

Australia, in 1986. Since 1987, he has been with The University of Adelaide, where he is presently a full professor in the School of Electrical and Electronic Engineering. His interests are in the areas of complex systems and multidisciplinary applications of physics and engineering. He has appeared on national and international television and radio and has also received scientific reportage in *New Scientist*, *The Sciences*, *Scientific American*, *Nature*, *The New York Times*, and *Sciences et Avenir*. He has more than 700 publications and has been an invited speaker at more than 100 institutions, including Princeton University, the Massachusetts Institute of Technology, the Santa Fe Institute, Los Alamos National Laboratories, Cambridge University, and EPFL, Lausanne, Switzerland. He won the GEC Bursary (1977), the Stephen Cole the Elder Prize (1998), the South Australian Tall Poppy Award for Science (2004), and the Premier's SA Great Award in Science and Technology for outstanding contributions to South Australia (2004). He has served as an editor and/or guest editor for a number of journals including *IEEE Journal of Solid-State Circuits*, *Chaos* (AIP), *Smart Structures and Materials* (IOP), *Journal of Optics B* (IOP), *Microelectronics Journal* (Elsevier), and *Fluctuation Noise Letters* (World Scientific), and he is currently on the editorial boards of *IEEE Photonics*, *Proceedings of the IEEE*, and *PLOS ONE*. He co-authored the books *Stochastic Resonance* published by Cambridge University Press and *Terahertz Imaging for Biomedical Applications* published by Springer. He co-edited the book *Quantum Aspects of Life*, with foreword by Sir Roger Penrose, published by Imperial College Press. Professor Abbott is a Fellow of the Institute of Physics (IOP) and is a Fellow of the Institute of Electrical and Electronic Engineers (IEEE).